Variability in spatial distribution of mineral phases in the Lower Bowland Shale, UK, from the mm- to μm-scale

Quantitative characterization and modelling

Fauchille, A. L.; van den Eijnden, A. P.; Ma, L.; Chandler, M.; Taylor, K. G.; Madi, K.; Lee, P. D.; Rutter, E.

DOI
10.1016/j.marpetgeo.2018.02.029

Publication date
2018

Document Version
Accepted author manuscript

Published in
Marine and Petroleum Geology

Accepted Manuscript

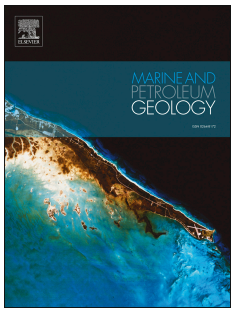

Variability in spatial distribution of mineral phases in the Lower Bowland Shale, UK, from the mm- to μm-scale: Quantitative characterization and modelling

A.L. Fauchille, A.P. van den Eijnden, L. Ma, M. Chandler, K.G. Taylor, K. Madi, P.D. Lee, E. Rutter

PII: S0264-8172(18)30075-8

DOI: 10.1016/j.marpetgeo.2018.02.029

Reference: JMPG 3257

To appear in: *Marine and Petroleum Geology*

Received Date: 18 October 2017

Revised Date: 12 February 2018

Accepted Date: 20 February 2018

Please cite this article as: Fauchille, A.L., van den Eijnden, A.P., Ma, L., Chandler, M., Taylor, K.G., Madi, K., Lee, P.D., Rutter, E., Variability in spatial distribution of mineral phases in the Lower Bowland Shale, UK, from the mm- to μm-scale: Quantitative characterization and modelling, *Marine and Petroleum Geology* (2018), doi: 10.1016/j.marpetgeo.2018.02.029.

Variability in spatial distribution of mineral phases in the Lower Bowland Shale, UK, from the mm- to µm-scale: quantitative characterization and modelling

Fauchille, A.L.[1,2,3*], van den Eijnden, A.P.[4], Ma L.[1], Chandler, M.[5], Taylor, K.G.[5], Madi, K.[6], Lee, P.D[1,2], Rutter, E[5].

[1]*Manchester X-Ray Imaging Facility, School of Materials, The University of Manchester, Oxford Road, Manchester M13 9PL, UK.*

[2]*Research Complex at Harwell, Rutherford Appleton Laboratory, Didcot Oxon OX11 0FA, UK.*

[3]*Ecole Centrale de Nantes, GeM-MEO, UMR 6183 CNRS, 1 rue de la Noë 44000 Nantes, France.*

[4] *Faculty of Civil Engineering and Geoscience, Delft University of Technology, Stevinweg 1, 2628 CN Delft, The Netherlands.*

[5]*School of Earth and Environmental Sciences, The University of Manchester, Oxford Road, Manchester, M13 9PL, UK.*

[6]*3Dimagination, Fermi Avenue, Harwell Oxford, Didcot, UK.*

**anne-laure.fauchille@ec-nantes.fr*

Resubmission for publication in:

Marine and Petroleum Geology

Abstract

The microstructure of a highly laminated Lower Bowland Shale sample is characterized at the micron- to millimeter scale, to investigate how such characterization can be utilized for microstructure-based modelling of the shale's geomechanical behavior. A mosaic of scanning electron microscope (SEM) back-scattered electron (BSE) images was studied. Mineral and organic content and their anisotropy vary between laminae, with a high variability in fracturing and multi-micrometer aggregates of feldspars, carbonates, quartz and organics. The different microstructural interface types and heterogeneities were located and quantified, demonstrating the microstructural complexity of the Bowland Shale, and defining possible pathways for fracture propagation. A combination of counting-box, dispersion, covariance and 2D mapping approaches were used to determine that the total surface of each lamina is 3 to 11 times larger than the scale of heterogeneities relative to mineral proportion and size. The dispersion approach seems to be the preferential technique for determining the representative elementary area (REA) of phase area fraction for these highly heterogeneous large samples, supported by 2D quantitative mapping of the same parameter. Representative microstructural models were developed using Voronoï tessellation using these characteristic scales. These models encapsulate the microstructural features required to simulate fluid flow through these porous Bowland Shales at the mesoscale.

Highlights

- The microstructure of the Lower Bowland Shale was studied quantitatively.
- The presence of multi-scale microstructural interfaces supports hydraulic fracturing potential in the Bowland Shale.
- The dispersion approach is the most suitable method to define representative elementary areas.
- 2D mapping of phase area fraction supports the dispersion approach.
- A representative model of the geometry of the microstructure based on Voronoï tessellation was generated.

1. Introduction

Significant shale gas and oil resources are believed to exist in Western Europe (EIA, 2013) and in particular in the UK (EIA, 2015a), such as in Carboniferous and Jurassic-Age shale formations. One example is the Bowland Basin, in the west portion of the Pennine Basin, close to Blackpool, Lancashire, Northern England (EIA, 2015). The Bowland Shale is generally divided into two units: the Upper Bowland Shale composed of thick layers of marine-deposited organic matter-rich mudstone, whilst the Lower Bowland Shale is composed of thinner alternating layers of organic-matter-poor and organic-matter rich mudstone (Andrews, 2013).

The Upper Bowland Shale demonstrates similarities to North American shale gas plays, whereas relatively few regions in the Lower part have been identified as potentially productive. The Lower Bowland Shale is still largely undrilled and its geographical extent is currently uncertain (Andrews, 2013). Despite this lack of data, the potential of the Lower Bowland Shale is considered to be important, albeit with a higher uncertainty than the Upper Bowland Shale (Andrews, 2013). Shale gas potential depends on the oil and gas retention capacity of the system, which is directly related to the microstructure: the nature and the specific adsorption of organic and inorganic phases, their structural relationships, and those of the pore and fracture networks. Moreover, quantifying the relationships between porosity, permeability, pore size distribution and brittleness in combination with the mineralogy and rock fabric is essential for the estimation of shale gas potential (Josh et al., 2012). Microstructural heterogeneities such as variations of grain size, shape, mineralogy, elasticity, anisotropy and stiffness, together with preexisting defects can create local stress concentrations. Such stress concentrations influence the initiation and behavior of fractures in shales, such as hydraulic fractures (Keneti and Wong 2010), mechanical fractures (Van de

Steen et al., 2003) and desiccation fractures (Hedan et al., 2012; Fauchille et al., 2016; Figueroa Pilz et al., 2017) in response to the local stress field. In a general sense, Sone and Zoback (2013) and Amann et al., (2014) have shown how significantly the microstructure can impact upon the mechanical properties of shale. As a direct result, the microstructure therefore influences the gas retention process (Bernard et al., 2010). Despite the strong interest in the Lower Bowland Shale in the UK, its petrophysical properties and heterogeneities are still poorly understood, but are expected strongly to influence yield during any gas production.

Due to the sub-micrometer scale of shale components, scanning electron microscopy (SEM) and transmission electron microscopy (TEM) are often used to characterize the microstructural features of shales (Ma et al., 2017). Houben et al., (2014, 2016) and Klaver et al., (2015) constructed mosaics of high resolution SEM images to quantify the morphology and size distribution of pores, clay and organic matter particles in the Opalinus Clay (Switzerland) and Posidonia Shale (Germany), and the microstructure of European Early Jurassic Shales. However, in light of the well-known heterogeneity of such rocks and the dependence of large-scale features (clay minerals, organics) on the structure of fine-scale features (clusters of inorganic grains, clay phase, fractures), the size of the field of view is often limited by the compromise between sample size and spatial resolution. Fracture initiation may depend on heterogeneities down to the nanometer scale if differential stresses are high enough, but fracture propagation is affected by multi-scale heterogeneities (Griffith, 1924; Jaeger and Cook, 1976). Consequently, the characterization of “low-scale” (meso- and macro-scales) heterogeneities should be considered in fracture propagation studies.

Mechanical behavior of shale at the macroscale is strongly dependent on the behavior at smaller scales, for example due to the primary structure and arrangement of particles (anisotropy), and also to the variability of small scale components such as organic matter,

rigid inclusions and clay minerals (Sayers, 1993; Wang, 2012; Wang et al. 2015, Bonnelye et al., 2017 a, b). As a consequence, understanding the microscale structure may aid detailed comprehension of the macroscale behavior and hence bulk constitutive relations. To predict strain location and fracturing behavior at the macroscale, simple models of grain-based microstructure taking into account microstructural parameters such as grain size, shape, proportion, elongation ratio and orientation ratio are required (van den Eijnden et al., 2015, 2016, 2017).

This study we investigates the variability of microstructural parameters (phase area fraction, grain size, shape, elongation and orientation) from the mm to µm scales in a sample of the Lower Bowland Shale, with a millimeter mosaic of SEM images at sub-micrometer resolution where two laminae were identified. The goals of the study are:

i) to quantitatively characterize the spatial variability of mineral phases of the Lower Bowland shale;

ii) to describe the heterogeneity of the microstructure using several methods allowing quantifications of representative elementary areas;

iii) to establish a simple representative model of the Lower Bowland shale microstructure based on the approach of van den Eijnden et al. (2015-2017), which takes into account (i) and (ii).

2. Geological Setting and Sampling

The Carboniferous Bowland Shale occurs across the center and north of England. Its occurrence extends from Merseyside to Humberside and Loughborough to Pickering (Andrews, 2013). It is divided into an upper unit with thick and continuous (a few hundreds of meter thick) shale formations, and a lower unit containing shale interbedded with clastic and carbonate deposits, explained by the influence of glacio-eustatic sea levels changes and

tectonic events (Gawthorpe, 1987; Andrews, 2013). For this study, one sample of Lower Bowland Shale was collected from the Preese Hall-1 borehole at a depth of 2495.27 meters, supplied by the British Geological Survey (BGS) in Nottingham (UK). The Preese Hall-1 borehole was drilled in 2010 on the Fylde coast of NW Lancashire at 53^{o} 49' 19.006"N; 2^{o} 56'56.576" near to Blackpool, north-west England. Preese Hall-1 was the first dedicated unconventional shale gas borehole drilled in the UK and Europe (de Pater and Baisch, 2011). The sample chosen for this study corresponds to sample B8 in Fauchille et al. (2017). The sample has a laminated microtexture and the mean organic content (TOC) is 1.1 wt %, measured with a Leco carbon analyzer using 100 mg powder samples, at the University of Newcastle (UK). Centimeter–size samples were used for making the powder samples, to ensure several laminae are included in the powder. According to bulk XRD measurements (the accuracy of quantification of XRD results in terms of modal proportions is around 1%), the sample is composed of 51.7 wt% quartz, 18.4 wt% kaolinite, 11.1 wt% ankerite, 8.6 wt% albite, 5.1 wt% muscovite, 3.5 wt% calcite and 1.6 wt% pyrite. The intact sample was vacuum impregnated with low-viscosity epoxy resin (Araldite 2020) at room temperature (20°C) and mechanically polished as a thin section with carbide and diamond products for scanning electron microscopy.

3. Methods Employed

3.1. Scanning electron microscope (SEM) mosaic image acquisition

A mosaic of 4×11 back-scattered electron (BSE) images each of 1280 × 960 pixels was acquired from the carbon-coated polished specimen at a resolution of 0.4 µm.pixel^{-1} (Jeol JSM-6610LV) with 23% overlap (Klaver et al., 2012; Vergès and Morales, 2014; Fauchille, 2015). The mosaic is 4204 × 8128 pixels (8bit) covering 1.68 × 3.25 mm^2. The working distance (WD) was 10 mm and the beam accelerating voltage was 20 kV. A magnification of

250X proved to be a good compromise between spatial resolution, field of view and acquisition time, and minimized drift of the incident electron beam and scanning lens. Contrast and brightness were adjusted to have the organic matter particles in black (0) and the heavy minerals in white (255). The parameters were optimized to obtain a histogram with distinct peaks to facilitate mineral segmentation (Prêt et al., 2010a; Robinet et al., 2012, Fauchille, 2015).

3.2. Correction and segmentation of images

All images were drift-corrected to produce a homogeneous histogram across all images of the mosaic. A linear gray level drift was observed in the *x* direction (horizontal) on each image, due to slight shadowing of the incident beam caused by the low-vacuum aperture of the pole-piece. Images were corrected in vertical sections of 30 × 960 pixels to balance the gray levels, producing consistent histograms with well-separated peaks (see Fig. 1). No significant shift was detected in the *z* direction (vertical).

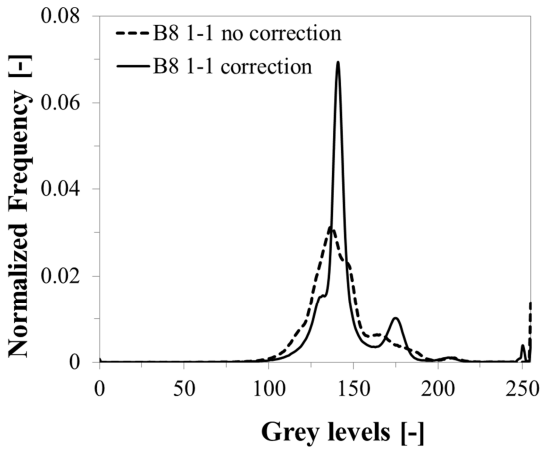

Fig. 1. Gray level histogram of the first image of mosaic B8 1-1 (this image corresponds to the first column and first line of the mosaic) before and after drift correction.

The mineral phases were segmented on the BSE images using a combination of filters and gray level thresholding using in-house codes written for Visual Studio, Matlab and ImageJ

(Peters, 2009; Prêt et al., 2010a,b; Robinet et al., 2012; Khan et al., 2014). The organic matter and fractures (om+fractures), feldspars (felds), ankerite, calcite (carb) and heavy minerals (h-min) were only segmented by gray levels with ImageJ. The gray levels used for thresholding were: 0 to 64 for organic matter and fractures, 65 to 133 for clays and quartz cement, 134 to 147 for quartz inclusions, 148 to 163 for micas, 164 to 192 for feldspars and ankerite, 193 to 218 for calcite and 219 to 255 for heavy minerals. Due to their similar silica contents, the segmentation of quartz and micas was performed using the gray level histogram and a local variance filter (Prêt et al., 2010a, Robinet et al., 2012). In ImageJ software, the value of the variance was chosen at 10 to detect the homogenous areas of quartz, according to the BSE images. Owing to the small size of kaolinite particles and their silica content being close to the background, clays were removed in the same phase as the quartz cement to form the "binder" of the sample. To improve the segmentation of individual grains, the 1-pixel boundaries of quartz and feldspars grains, were moved to the background. This implies that the segmentation of grains may be underestimated but better separated for calculating morphological parameters. The segmentation, shown in Fig. 2 takes into account the separation between the large grains of quartz and the cement, but cannot differentiate between organic matter particles and fractures, both of which present the same gray scale value (black) on BSE images. The fractures segmented on the mosaic are filled by organic matter or empty. Fractures can be generated by pore fluid overpressuring through organic decomposition and petroleum generation, by the late migration of organic matter. Open cracks can be produced as a result of sample depressurization during recovery and during the sample preparation (Fauchille et al., 2017). There is a fracture filled by ankerite (top right part in Figure 2), which was therefore segmented as ankerite minerals (carbonates).

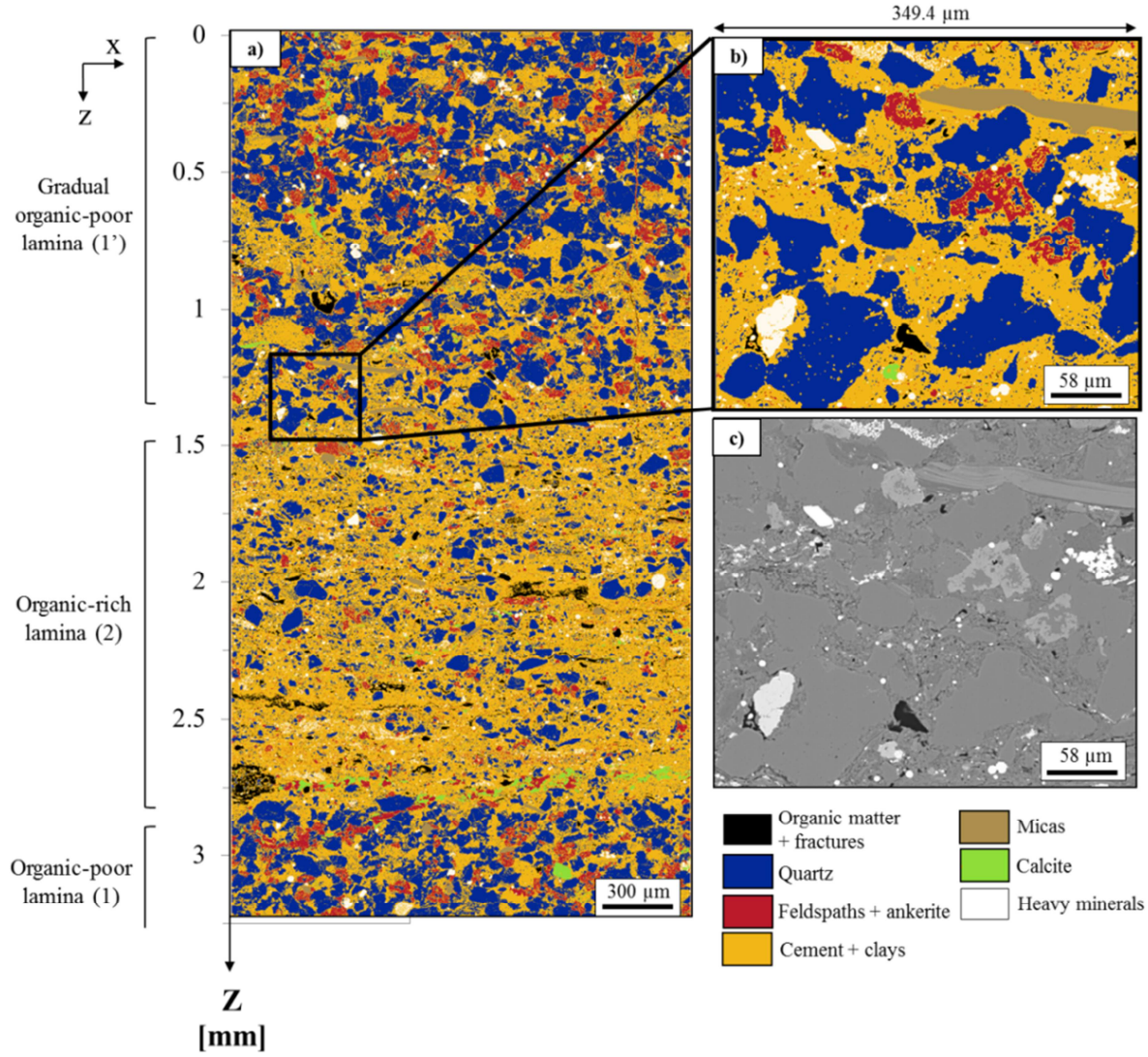

139

140 **Fig. 2. (a) Mineral phase segmentation on the whole mosaic of SEM-BSE images of the**
141 **Bowland Shale sample. (b) Magnified view of a region of (a). (c) Original**
142 **(unsegmented) back-scattered electron image corresponding to (b).**

143 ## 3.4. Image analysis

144 ### Microstructural parameters

145 The anisotropy of the microstructure was studied using the 2D microstructural parameters
146 used on shale (Robinet et al., 2012; Fauchille et al., 2014, 2016). These are the area fraction
147 (ratio between the number of pixels of a grain type and the total number of pixels in the

calculation window), the grain size (number of pixels in one grain), the elongation ratio and the orientation, calculated with the ellipsoid plugin in ImageJ software. The ellipsoid axial ratio and orientation of each grain with respect to the reference horizontal axis was calculated, but only for grains larger than 10 pixels, in order to avoid any resolution artefacts.

Determination of correlation lengths of the microstructure

The estimation of a representative elementary area (REA) (also called homogenization surface) of a material for a specific property, scale and resolution (Bear, 1972; Bear and Bachmat, 1984; Grolier et al., 1991; Al-Raoush et al., 2010), can be problematic in shales due to their well-known multi-scale and multi-modal heterogeneities. However, the characterization of heterogeneities and the identification of REAs are crucial for upscaling and modelling studies. In theory, a surface is representative of a parameter at a specified scale when this parameter becomes independent of the size of the field of view, including statistically all types of structural heterogeneities (Bear, 1972; Kanit et al., 2003; Al-Raoush et al., 2010). In this paper, three methods were used and compared to estimate representative elementary surfaces of the microstructure and to identify its heterogeneities: (i) the counting-box method, (ii) the dispersion approach, and (iii) the covariance. All calculations were performed with in-house codes in Visual-Studio (C) and Matlab. Other methods and parameters were used to extract correlation lengths from an image, such as the entropy method (Boger et al., 1992) and the percolation method (Cosenza et al., 2015), but they are not taken into account in this paper.

Counting box method

A simple way to approximate the REA is the “counting-box method”, that considers a succession of increasing-size domains until the parameter measured is constant (VandenByggaart and Protz, 1999; Kameda et al., 2006; Houben et al., 2014), plus or minus a

defined confidence limit which was chosen to be 10% in our case, consistent with previous studies on geological materials (VandenByggaart and Protz, 1999; Houben et al., 2014; Vik et al., 2014). In this study, each lamina was defined over an area of 4404 × 3302 pixels (1.76 × 1.32 mm), and the domains between 10 × 10 pixels (4 × 4 µm) to 3302 × 3302 pixels (1.32 × 1.32 mm) were used for this method. The first domain was chosen in the center of each lamina, in order to have the maximum number of possible domains.

Dispersion approach

The dispersion approach was introduced by Kanit et al., (2003). Applied to a 2D image, it involves dividing the image into equal subsamples, in which a chosen parameter is calculated. The goal of this approach is to determine the number of subsamples needed limit to an acceptable level the relative error of this parameter for the set of subsamples.

The mosaic of BSE images was divided into independent square domains *D* from 10 × 10 to 1876 × 1876 pixels (4 × 4 and 750 × 750 µm^2, respectively) (Kanit et al., 2003; Keller et al., 2013). Kanit et al., (2003) used this approach to divide random and Voronoï mosaics into a finite number of cells. In this paper, the domains D are the finite square cells of the experimental mosaic. This mosaic cannot be extended therefore the number of D decreases as their size increases. Each domain is thus a subsample of the mosaic and contains a finite number of grains. The pixels of the domains are independent from one domain to another, but it is possible that long or large grains (such as micas, Fig. 2b) can be included in multiple neighboring domains. The standard deviation, $\sigma_{D,}$ of the phase area fraction $P_D(x,z)$ on each lamina as a function of domain size *D* was used to quantify the heterogeneity of the microstructure (Equations 1 and 2) with a statistical approach.

$$P_D\,(x,z) = \frac{1}{D} \sum_{n=x-\frac{D-1}{2}}^{n=x+\frac{D-1}{2}} \sum_{m=z-\frac{D-1}{2}}^{m=z+\frac{D-1}{2}} G_{(n,m)} \quad (1)$$

$P_D(x,z)$ is the area fraction of a defined phase (examples: carbonates, quartz, cement/clays…) in a domain, *D*, centered at (*x*,*z*). $P(x,z)$ varies between 0 and 1. *D* is the size of the domain in pixels (and is always an odd number). G is a binary function (0 or 1). G = 1 when the pixel (*n*, *m*) corresponds to the chosen phase, and 0 when the pixel corresponds to a different phase. For example, when the area fraction of calcite is calculated: $G_{(n,m)}$ =1 if the pixel (*n*, *m*) corresponds to calcite, and 0 if the mineral is not calcite.

To have a whole view of the dispersion of area fraction values, $P_D\,(x,z)$ was mapped in 2D increments by 1 pixel in the *x* and *z* directions over the mosaic. The standard deviation σ_P of $P_D(x,z)$ was then calculated as a function of domain size (Equation 2):

$$\sigma_P = \sqrt{\frac{\sum(P_D(x,z) - \overline{\overline{P_D}})^2}{N_D}} \quad (2)$$

$\overline{\overline{P_D}}$ is the mean value of the phase area fraction in all domains *D* and N_D is the number of domains D.

This dispersion approach allows us: (i) to identify the minimum size of a representative area of area fraction with $\sigma_P < 0.1$; (ii) to map in 2D the area fraction to present a direct visualization of microstructural variability and its multi-scale heterogeneities; and (iii) to investigate the evolution of the variance ${\sigma_P}^2$ as a function of *D* in order to estimate the effect of the randomness of the microstructure on the whole mosaic. The characterization of

heterogeneities and REAs will be used for microstructural modelling afterwards. Other parameters of grains, such as the size, the representative ellipse axial ratio or its long axis orientation can be investigated to map the spatial variability of microstructure, but the area fraction was chosen here as a good indicator of the microstructure, and it is commonly used in 2D and 3D texture analysis (VandenByggart et al., 1999; Madi et al., 2005; Houben et al., 2014; Fauchille, 2015; Klaver et al., 2015).

Covariance

The covariance approach is commonly used to determine characteristic scales and to quantify the anisotropy of 2D microstructure (Berryman and Blair, 1986; Stoyan et al., 1995; Jeulin, 2001; Kanit et al., 2003; Degallaix and Ilschner, 2007; Rolland du Roscoat et al., 2007; Rudge et al., 2008; Gaboreau et al., 2016). The principle of covariance is the measurement of how well one image matches a spatially shifted copy of itself. The covariogram $C(X,h)$ measures the intersection of a 2D image X and the translated image of X by a distance h (Kanit et al., 2003) (Equation 3):

$$C(X,h) = \int c(x)c(x+h)\,dx \qquad (3)$$

where $c(x)$ is the phase detection function, defined by :

$$c(x) = \begin{cases} 1\ if\ x \in X \\ 0\ \ else \end{cases}$$

The dispersion of the state of two points x_1 and x_2 between the image X and the image X translated by h can therefore be quantified (Kanit et al., 2003). For a non-periodic microstructure, correlations between points decrease with increasing h. When h is sufficiently large, there is no correlation anymore between the points of the two images. Consequently, $C(X,h)$ describes an asymptotic behaviour limited at the mean phase

proportion, $\bar{P}^2$, of the whole image. When the asymptote is not reached, the points included in the image are partially correlated, and therefore the image size is not considered to be representative of its content. The distance h corresponding to the scale beyond which the asymptote matches will be therefore considered as an indicator for defining an adequate scale of microstructure. The covariograms of the parts corresponding to each lamina (independent areas of 4404 × 3302 pixels) were calculated. All phases were first considered independently in the calculation.

3.5. Numerical model for microstructure and mineral geometry

A simple model for convex grains, based on Voronoï diagrams (Sellers and Napier, 1997; Fan et al., 2004; van den Eijnden et al., 2015, 2017) is used to reproduce the microstructure. Previously this model has been used to generate simple microstructures in a periodic representative elementary volume with straightforward finite element discretization (van den Eijnden, 2015), and to model the microstructure of a Callovo-Oxfordian claystone (van den Eijnden et al. 2017). Here, the model is used to investigate microstructures with geometrical properties matching those of the different laminae of the studied Bowland shale. The model applies Voronoï tessellation on a set of randomly generated sites and uses the resulting diagram as a geometrical model of the microstructure. Preferred orientations and grain elongation are introduced by stretching the domain during tessellation by an amount ξ which thereby becomes a model parameter for the grain shape contribution to total anisotropy. The model calibration is by a minimization of the root-mean-square error between the model distributions and experimental distributions of total grain elongation L and orientation β (see Fig. 6). As the model is based on Voronoï tessellation, there is little flexibility in the grain size distribution without a strong distortion of the grain geometry distributions. For this reason, no attempt was made to reproduce the grain size distributions, and the emphasis here is on reproducing the correct distributions of (1) elongation (also called length ratio), (2)

grain orientation and (3) area fraction of all mineral groups (including organic matter and fractures). Calibration of the model has indicated that grain circularity corrections, as part of the model in van den Eijnden et al., (2017), are not needed to capture the grain geometry distributions of the shale.

Distributions of grain orientation and elongation for the different mineral types can be reproduced reasonably well using simple Voronoï tessellation while slight manipulation of the sites and stretching of the domain is applied during the tessellation operation. Based on the parameter distributions and area fractions of the different mineral types, mineral properties can be assigned. Their parameter distributions are then approached in the model.

The distributions of orientation and elongation are matched in an average distribution of all phases combined (quartz, carbonates, feldspars, micas, heavy minerals, organics and fractures). In the microstructure model, the phases are scattered as a function of their experimental area fraction. The cement and clays were first divided into random cells but their boundaries were then merged to form a unique phase. van den Eijnden et al., (2017) provide further details on the method of developing the microstructure model.

According to the experimentally determined area fraction of mineral phases, the mineral types were assigned following the conditional probability $P_M(m_i|L,\beta)$ to meet specified orientation and elongation properties, matching the distributions in Fig. 11. m_i is the type of mineral phase, L the elongation and β the orientation, which is the direct application of Bayes' theorem to derive a conditional probability, with an additional correction factor to account for grain-size dependency of the model (Bernardo and Smith, 2001; Berger, 2013). This probability is defined by Equation 4:

$$P_M^N(m_i|L,\beta) = \frac{q_D^N(L,\beta|m_i) f_D^S(m_i)}{q_M^N(L,\beta)} c_i \quad (4)$$

with $f_D^S(m_i)$ being the area fraction of mineral phase m_i (following Table 1), $q_D^N(L,\beta|m_i)$ is the bivariate distribution of L and β in the data for phase type m_i and $q_M^N(L,\beta)$ is the bivariate distribution of L and β of all phases in the model. c_i is a ratio to correct for the influence of the correlation between grain size and grain geometry in the model on the final area fractions of the minerals. The values of c_i are defined theoretically as the ratio of the resulting model area fraction over the expected area fraction of the assigned materials, and requires the distribution of model grain size as a function of L and β. However, here the ratios c_i have been determined based on the resulting area fractions of the model and updated iteratively to obtain the required area fractions. Values for c_i range between 0.6 and 1.25.

4. Results

4.1. Vertical variability of phase content

Fig. 3 shows the vertical variation of all area fractions, for independent horizontal domains of 200 µm × 1.682 mm. A width of 200 µm was chosen as a good compromise to show quantitatively the vertical variability of area fractions including different types of microstructural heterogeneities.

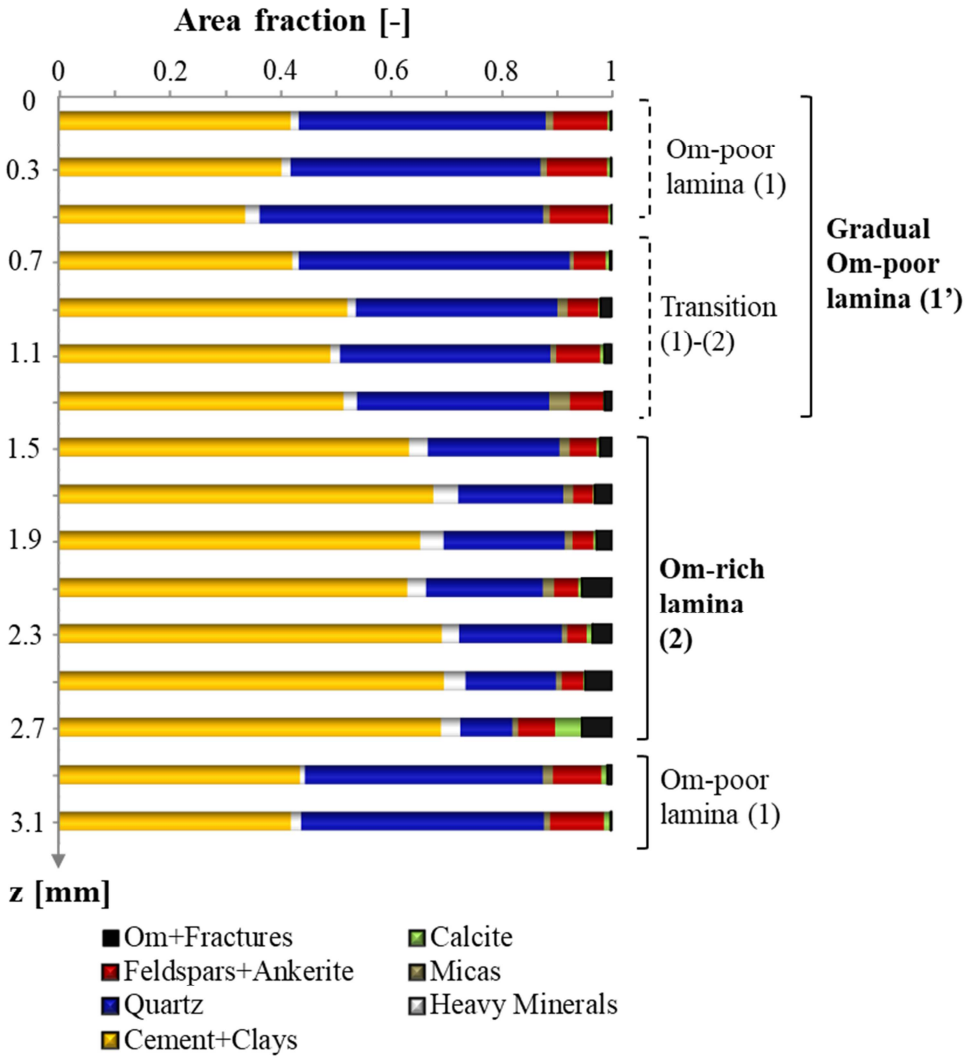

292

293 **Fig. 3. Vertical variability of the area fraction of each mineral along the z axis of the**
294 **mosaic, based on horizontal domains of 500 × 4204 pixels (200 µm × 1.682 mm).**

295 Three different regions were identified:

296 **(1) Organic-poor laminae** (z = 0-0.80 mm and z = 2.8-3.25 mm). These laminae are
297 characterized by an area fraction of cement and clays lower than 50 % with a near zero
298 content of organics and fractures. The detrital quartz grains represent 40 to 50 % of area, and
299 heavy minerals (mostly pyrite), micas and calcite are on the order of a few percent. The
300 proportion of feldspars and ankerite is around 8-10 %.

(2) Organic-rich lamina (z = 1.4-2.8 mm). This lamina is 1.4 mm thick, and composed of 60 to 70 % of area as cement and clays with a higher organic and fracture content between 1.7 to 7 %. The proportion of detrital quartz is between 10 and 30 %. The heavy mineral content is also higher than in the organic-matter poor lamina with variable proportions between 2 and 5 %. Feldspars and ankerite are less common with area fractions between 2 and 6 %. Calcite and micas are still scarce, although peaks of micas and calcite were detected due to very large micas at z = 1.2 mm and the presence of an horizontal calcite vein at z = 2.7 mm.

Transition (1)-(2): This is the transition between organic-poor and organic-rich laminae (z=0.80-1.4 mm). It is marked by a progressive increase in cement and clay area content from 40 to 62 %, and a decreasing proportion of detrital quartz grains from 50 to 30 %. Feldspars/ankerite variability is less marked at between 6 and 2 %. The proportion of heavy minerals increases from 2 to 5 %. However, the transition between the organic-poor and the organic-rich laminae around z = 2.8 mm is very abrupt with sharp jumps in cement/clays, organic-matter/fractures, quartz and heavy mineral proportions. The proportion of cement/clays falls from 70 to 38 % over 240 µm (between z = 2.68 to 2.92 mm), while quartz content dramatically increases from 9 to 49 % in 220 µm (between z = 2.76 to 2.92 mm).

In order to ensure a sufficient dataset for statistics in sections 4.3 to 4.5 below, the organic-poor and one part of the transition (z = 0-1.28 mm) zones were taken together to form a gradual organic-poor lamina (1'), in order to compare its microstructure with the that of the organic-rich lamina (2) (z = 1.48-2.76 mm).

4.2. Spatial variability of phase content

2D maps of P are shown as Fig. 4 for cement and clays, quartz, feldspars and carbonates, and organics and fractures for N = 200, 500, 1250 and 1876 pixels, i.e. for, 80, 200, 500 and 750

µm respectively (Fig. 4). $P = 1$ means that the domain D consists 100 % of the phase considered whereas 0 (purple) means it is completely absent.

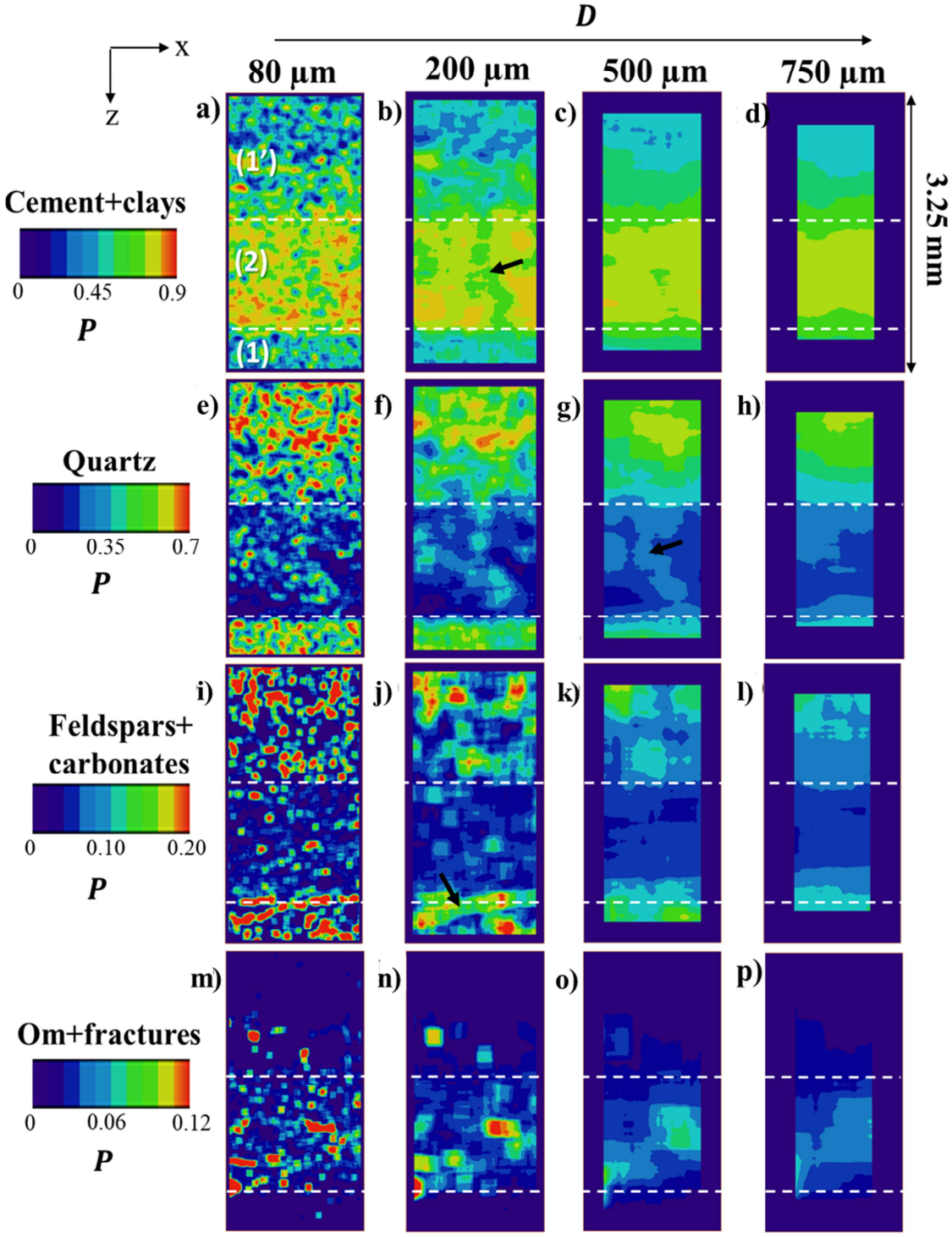

Fig. 4. 2D maps of phase area fractions with variable domain sizes for: (a-d) cement+clays, (e-h) quartz, (i-l) feldspars+carbonates, (m-p) Om+fractures. [Each of

the three laminae [(1) organic-poor lamina, (1') gradual organic-poor lamina, (2) organic-rich lamina] are labelled on (a).

The organic-rich lamina 2 is clay and cement-rich, and detrital quartz, feldspar and carbonate-poor (Fig. 4 a-l). The organic-matter and fractures are heterogeneously distributed due to the variable sizes of particles and fractures (Fig. 4 m-p). The organics and fractures are nearly absent in the organic-poor lamina (1) (Fig. 4 m-p). The gradual organic-poor lamina 1' is quartz, feldspar and carbonate-rich (Fig. 4 e-l). The heterogeneities relative to *P* are defined by local higher or lower phase area fraction than the mean phase area fraction of each map (local concentration of red or blue colors for example). For all phases and *D* sizes, the area fraction is spatially heterogeneous in *x* (horizontal) and *z* (vertical) directions on the whole mosaic, mainly due to the presence of a sedimentary lamination (Fig. 2a), but also to a heterogeneous distribution of mineral phases inside each lamina.

For $D = 80$ µm, local high concentrations of quartz, feldspars, carbonates and organics (red areas in Fig. 4 e,i,m, first column) defined the grain shapes visible on the mosaic in Fig. 2. The phase heterogeneities are thus relative to the grain-size scale for $D = 80$ µm, due to the small value of *D* including a low number of grains. Therefore this scale shows interfaces between relatively large grains and the phase including cement and clays. For $D = 200$ µm, the organic-rich lamina contains circular clay and cement-rich areas and a discontinuous vertical line with a lower concentration (Fig. 4b), mainly due to the presence of quartz (Fig. 4f). Scattered feldspar and carbonate-rich areas were detected in the gradual organic-poor lamina with a concentration gap around 0.15-0.20 with respect to the background. However, the organic-poor lamina contains a continuous line with a higher concentration of feldspars and carbonates ($P > 0.15$), mainly due to the presence of calcite veining (black arrow in Fig. 4j) . This scale highlights the areas rich in large particles of organics and large fractures in the organic-rich lamina (Fig. 4n). The maps show these interfaces between clusters and grain-

poor areas with the background at the scale of $D = 200$ µm. For $D = 500$ µm, cement and clay proportion heterogeneities are averaged, reducing their surface fractions in both laminae (Fig. 4c), whereas larger clusters of feldspars, carbonates, and quartz are highlighted (Fig. 4 g, k). A continuous vertical line of quartz ($P > 0.25$) is present in the organic-rich lamina (black arrow in Fig. 4g). The organics and fractures are divided in two separate clusters with $P > 0.06$ in the organic-rich lamina (Fig. 4o). For $D = 500$ µm, the domains D contain thus more grains and average the phase area fraction and their heterogeneities relative to individual and clusters of grains at larger scales than $D < 500$ µm. For $D = 750$ µm, phase area fraction maps show the progressive and abrupt transitions between the different laminae (Fig. 4 d, h, l, p, last column). They highlight the interfaces between sedimentary laminae, and the maps for $D = 500$ show heterogeneities for extended clusters and the beginning of the detection of laminae at an intermediate scale between $D = 200$ and 750 µm.

The multi-scale mapping of phase area fractions shows three different types of microstructural heterogeneities relative to three different scales: (i) the interfaces between rigid inclusions (quartz, feldspars, carbonates, organics) and the phase cement/clays, (ii) the interfaces between clusters of rigid inclusions and the background and (iii) the interfaces between laminae. These maps highlight the high multi-scale variability of microstructure, based on the area fraction parameter.

4.3. Variability of microstructural parameters

The grain size, grain number per size, length ratio and orientation of grains were calculated for each of laminae 1' and 2 (labelled on Fig. 4a) in independent areas of 4204 × 3200 pixels (1.682 × 1.280 mm^2) (Fig. 5).

Variability of grain size

The grain size distribution (GSD) is an important parameter to help understand the sedimentation conditions. As expected in shale, the grain size distributions (Fig. 5 a, b, c), follow a power-law for both laminae for quartz, feldspars, carbonates, organic matter and fractures, micas and heavy minerals (not shown). Their fractal dimensions on the studied areas are shown. In both laminae 1' and 2, the GSD of feldspars, carbonates and quartz are similar for grain surfaces below 200 pixels (Fig 5 a, c) and differ significantly above 200 and 300 pixels respectively, especially for feldspars and carbonates (Fig. 5a). This difference is interpreted as a result of a large proportion of large grains (surface above 200 pixels) of feldspars and carbonates in the organic-poor lamina (Fig. 5b) alongside the presence of grain clusters (aggregates of grains, red grains in Fig. 2a). The GSD for feldspars and carbonates describes a dual power law, thus large grains and clusters contribute heavily to the total phase proportion of the gradual organic-poor lamina. Quartz GSD differ for grains larger than 200 pixels but the effect is less pronounced than in feldspars and carbonates (Fig. 5c), whereas quartz clusters are more easily visible in Fig. 2 (blue grains). The number of independent quartz segments is fewer by 18 % in the gradual organic-poor lamina 1' than the organic-rich lamina 2 (Fig. 5d), despite Fig. 2a suggesting the opposite. This can be explained by the fact that the quartz clusters are significantly larger than the feldspar and carbonate clusters, hence their number and frequency are consequently much lower. In the gradual organic-poor lamina 1', quartz regions are relatively small and independent, whereas they are larger and arranged in clusters in the organic-rich lamina 2. The clusters decrease the number of individual quartz segments, which minimize their impact on the GSD (Fig. 5 c,d).

Organic matter and fractures show very close GSD for both laminae 1' and 2 (Fig. 5 e) but the number of segmented features is until 4.8 times higher in the organic-rich lamina 2 than the gradual organic-poor lamina 1' (Fig. 5 d).

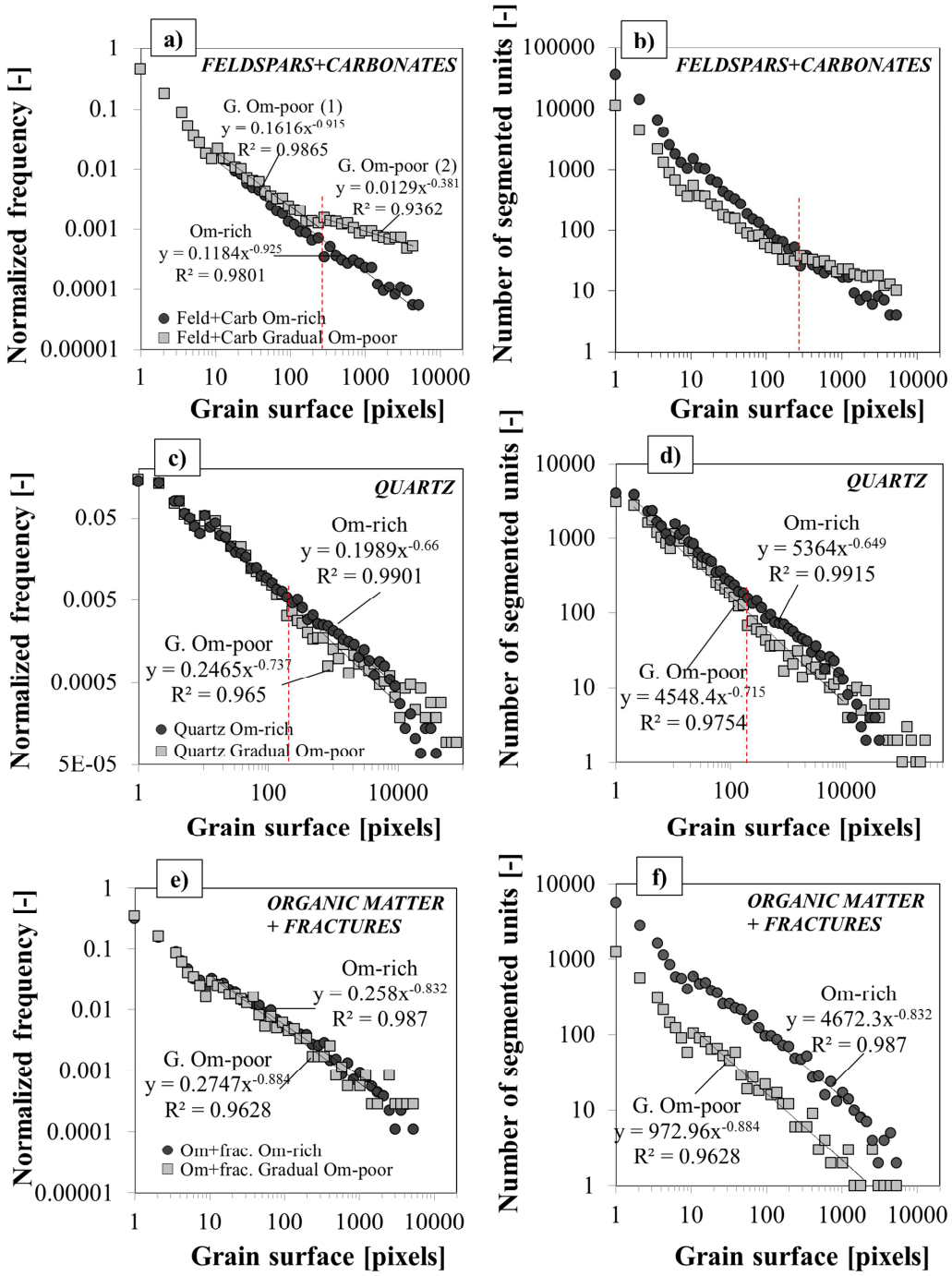

402

403 **Fig. 5. Grain size and grain number distributions for each of laminae 1' (gradual om-**

404 **poor) and 2 (om-rich).**

405 ***Variability of anisotropy***

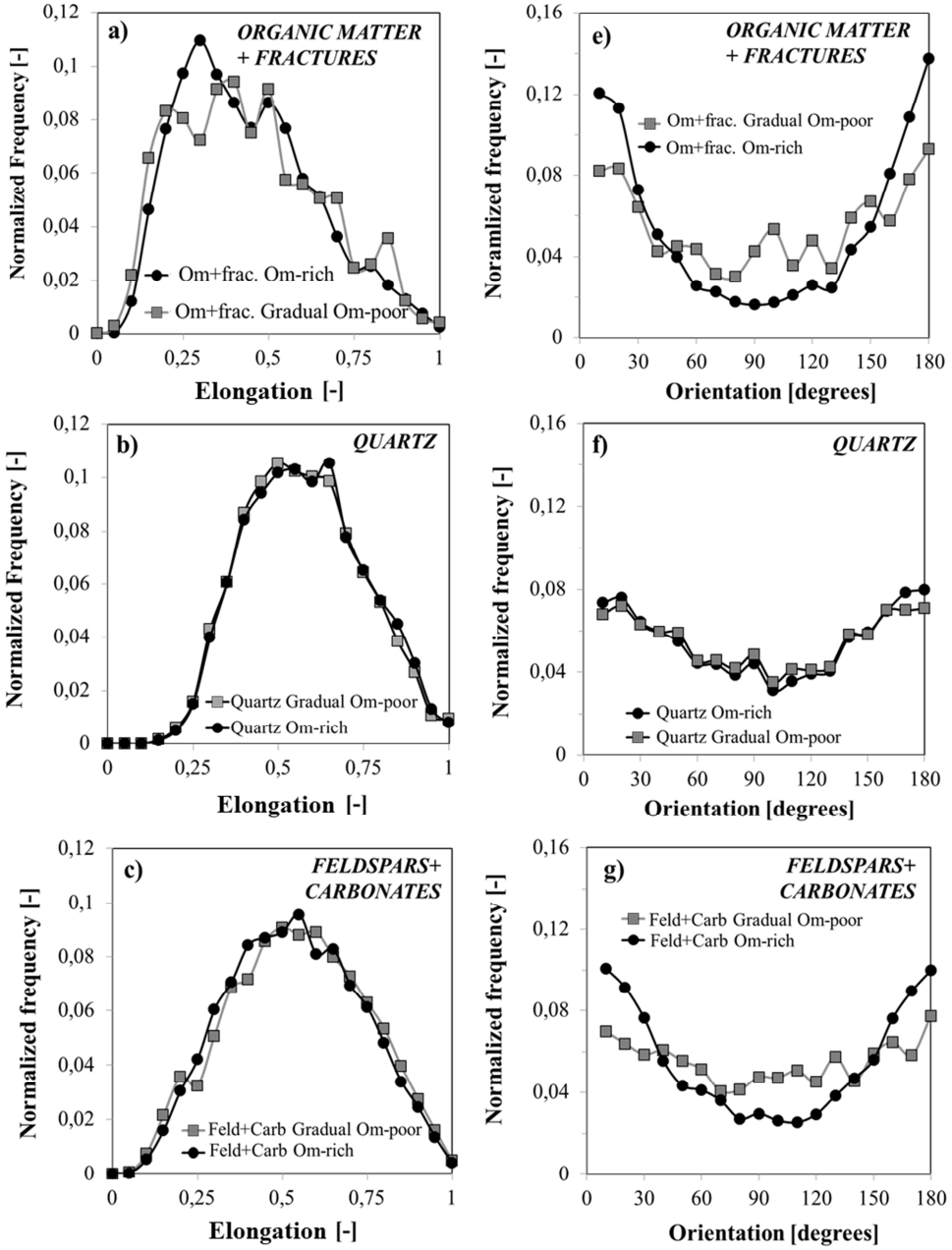

406

407 **Fig. 6. Elongation and orientation distributions for a), b) organic matter particles and**
408 **fractures, c), d) quartz, e), f) feldspars and carbonates, on the organic-rich (black plots)**
409 **and the gradual organic-poor (gray plots) laminae 2 and 1' respectively. Only grains**
410 **larger than 10 pixels were considered.**

For both laminae, the microstructure of the Bowland Shale sample is anisotropic due to horizontally-elongated quartz, feldspars, carbonates, organic matter particles and fractures (Fig 6 a-g). The elongation distributions of quartz, feldspars, carbonates, organics and fractures do not change significantly between the gradual organic-poor and the organic-rich laminae (Fig. 6 a,b,c). However, the orientation distribution of organics, fractures, feldspars and carbonates differ between the organic-rich lamina to the gradual organic-poor lamina (Fig. 6 e,g). Organics, fractures, feldspars and carbonates are more elongated horizontally (long-axis highest orientations at 0 and 180 degrees, i.e. parallel to the trace of bedding) in the organic-rich lamina contrary to detrital quartz minerals which do not show any variation of orientation between the two laminae (Fig. 6f). Based on these two criteria, the variation of anisotropy is mainly due to a variation of orientation of fractures and feldspars, carbonates, organic matter particles and fractures. Note that this measure of anisotropy ignores contributions from any preferred crystallographic orientation of grains (other than micas) that might exist and oriented cracks smaller than microscopic resolution.

4.4. Quantitative description of the microstructure

Figs. 3 to 6 have shown that the microstructure is spatially variable. However, even if the microstructure is variable, microstructure modelling is required to predict strain localisation and potential sites of fracture initiation in rocks (Lan et al., 2012; van den Eijnden et al., 2016). In this section, three methods are used to quantify representative elementary areas of the measured microstructure, based on the surface proportion of phases, and as applied to polycrystalline and heterogeneous materials (Kanit et al., 2006; Madi et al., 2005) and rocks (Klaver et al., 2012; Houben et al., 2014; Vik et al., 2014). These methods can quantify how representative are the microstructural models generated from the microstructural parameters of the mosaic.

Counting-box approach

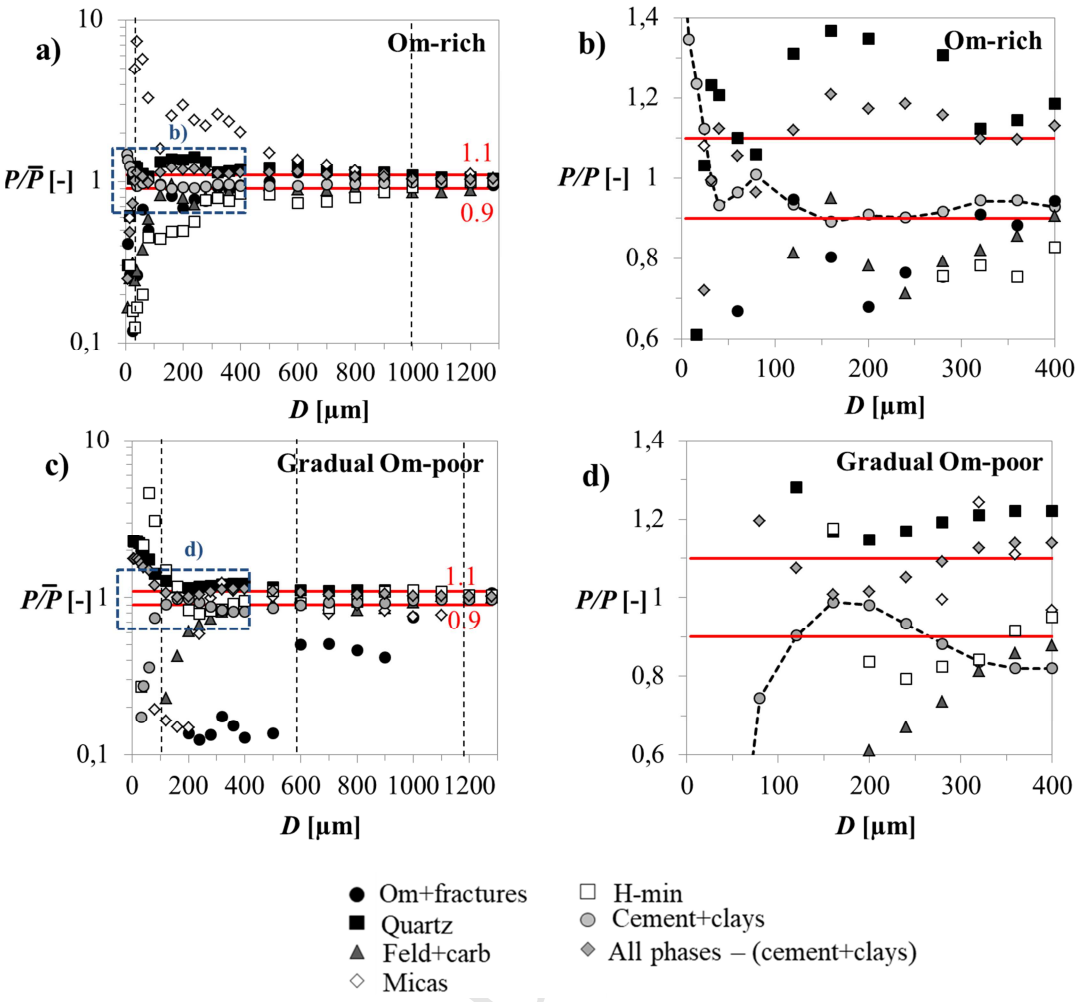

436

437 **Fig.7. (a and b) Ratio between the local phase area fraction *P* and the mean phase area**
438 **fraction $\bar{P}$ as a function of the size of calculation domain *D* for the *organic-rich lamina***
439 **where b) is a magnified view of the dashed-line box in a) for *D*≤400µm. (c and d) show**
440 **similar features for the *gradual organic-poor* lamina, where d) is a magnified view of the**
441 **dashed-line box in c) for D≤400µm.**

442 The starting point of the counting box method is the center of each lamina image, in order to
443 take into account the maximum number of different *D* values. *P* is the mean area fraction of
444 the phase in *D* and $\bar{P}$ is the mean phase area fraction in the whole image of the lamina. In the
445 organic-rich lamina, the ratios $P/\bar{P}$ for cement-clays (gray circles in Fig. 7 a,b) and all rigid
446 inclusions (gray diamonds in Fig. 7a,b) start to oscillate at 1±0.10 for *D* close to 50 µm and

320 µm, respectively. However, the ratio $P/\bar{P}$ of all phases separately considered is stable at 1±0.10 for $D \geq 1$ mm. This result is interpreted as being a balance effect between the different mineral phase fractions. In the gradual organic-poor lamina 1' (Fig. 7 c, d), $P/\bar{P}$ varies at 1±0.10 for $D \geq 120$ µm for the cement-clays (oscillation around 0.9) and the overall grain phase (oscillation around 1.1). However, all phase area fractions taken independently are stable for $D \geq 600$ µm, except organics and fractures at $D \geq 1.1$ mm due to small and elongated units (Fig. 5f, 6d) and a low mean area fraction on the whole image. Consequently, $P/\bar{P}$ reaches 1±0.10 for $D \geq 1.2$ mm for all phases separately considered. The homogenization areas are larger for the gradual organic-poor lamina than the organic-rich lamina due to higher grain sizes and larger clusters, and the scattering of small and low frequency phases such as organics and fractures.

Dispersion of phase proportion

Each lamina was divided into a number, N, of independent domains, D, to calculate the standard deviation $\sigma_P(D)$, variance ${\sigma_P}^2(D)$ and relative error $\varepsilon_{rel}(D)$ (Fig. 8) of each phase area fraction *P* as a function of *D* (Kanit et al., 2003) (Equation 5, Fig. 8, Tables 1,2). :

$$\varepsilon_{rel}(D) = \frac{2\sigma_P(D)}{\bar{P}\sqrt{N}} \quad (5)$$

with $\bar{P}$ the mean phase area fraction between 0 and 1.

In Kanit et al., (2003), *N* is the number of cells on theoretical Voronoï mosaics. In this study, *N* is the number of cells, called domains, of the experimental mosaic. A domain can therefore be considered as a 2D rock subsample of the whole mosaic of the Bowland Shale. The experimental mosaic has a limited size, so the number of domains is also limited to a finite value.

The fitting of relative uncertainty ε_{rel} by a power law $\varepsilon_{rel} = a.D^{-b}$ (Table 1) allows the quantification of ε_{rel} for the surface corresponding to each type of lamina (Fig. 8, table 1). On each lamina, the number of calculation domains as a function of the domain's size follows the law: $N = 2.10^6.D^{-b}$ with $b = 2.05$ ($r^2 = 0.9993$) for D between 10 and 1250 pixels (4 and 500 µm respectively). Data with fewer than 10 domains were not considered (Kanit et al., 2003), i.e domains above 400 µm. As expected, the dispersion of P decreases when the size of D increases for phases segmented. The relative errors of all phase area fractions were calculated as a function of D for both laminae according to equation 5 (see Figure 8).

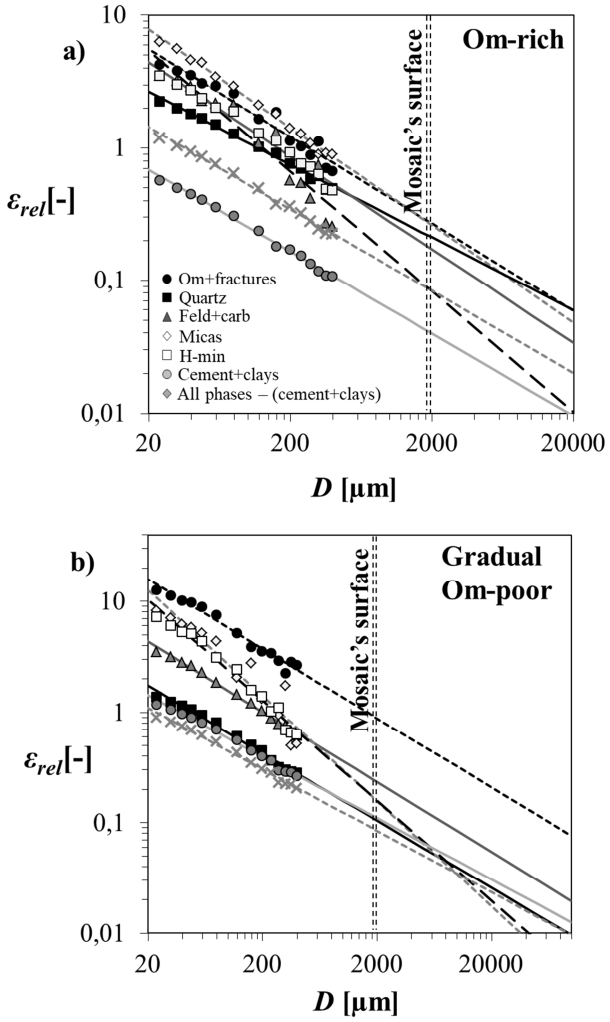

Fig. 8. Relative uncertainty, ε_{rel}, of area fraction as a function of D for a) the organic-rich lamina and b) the gradual organic-poor lamina, for $N = 1$.

Considering all phases combined together in both laminae, $\varepsilon_{rel} = 0.11$ and 0.09 for square domains of 1.32×1.32 mm^2 and 1.76×1.76 mm^2 respectively (gray crosses in Fig. 8), whereas $\varepsilon_{rel} \gg 0.1$ for the phases segmented independently for same *D*. Based on the surface proportion, the areas used to characterize the lamina's microstructures are representative with a ε_{rel} around 10% when all mineral phases are considered together in a unique phase, but not separately, at the study resolution.

Gradual Om-poor	**a**	**b**	**R^2**
Om+fractures	103	0.626	0.97
All grains	5.80	0.556	0.99
Cement+clays	7.54	0.556	0.99
Quartz	10.8	0.610	0.99
Feldpars+Carbonates	29.1	0.635	0.99
Heavy minerals	154	0.906	0.98
Micas	218	0.952	0.90
Om-rich			
Om+fractures	39.8	0.658	0.95
All grains	9.19	0.619	0.99
Cement+clays	4.39	0.619	0.99
Quartz	13.9	0.551	0.99
Feldpars+Carbonates	81.9	0.908	0.91
Heavy minerals	36.6	0.706	0.99
Micas	71.3	0.738	0.99

Table 1. Parameters of the power law fitting, ε_{rel}, as a function of *D* corresponding to both laminae.

		REA [mm]								
		N=1			N=5			N=10		
	ε_{rel}	***0.15***	***0.1***	***0.05***	***0.15***	***0.1***	***0.05***	***0.15***	***0.1***	***0.05***
Organic-rich	Cement+clays	0.233	0.449	1.38	0.063	0.122	0.375	0.036	0.070	0.214
	Grains	0.746	1.44	4.40	0.203	0.391	1.20	0.116	0.223	0.685
	Quartz	3.71	7.75	27.2	0.861	1.80	6.33	0.459	0.959	3.37
	Feld+Carb	1.03	1.62	20.4	0.426	0.666	1.43	0.291	0.455	0.975
	H-min	2.41	4.28	11.4	0.771	1.37	3.65	0.472	0.838	2.24
	Om+fractures	4.83	8.94	25.6	1.42	2.63	7.55	0.839	1.55	4.46
	Micas	4.24	7.35	18.8	1.42	2.47	6.32	0.892	1.54	3.95
Gradual Organic-poor	Cement+clays	1.15	2.38	8.28	0.270	0.560	1.95	0.145	0.300	1.04
	Grains	0.715	1.482	5.16	0.168	0.349	1.21	0.090	0.187	0.650
	Quartz	1.10	2.14	6.68	0.295	0.573	1.79	0.167	0.325	1.01
	Feld+Carb	4.02	7.61	22.7	1.13	2.14	6.38	0.655	1.24	3.70
	H-min	2.12	3.32	7.14	0.874	1.37	2.94	0.596	0.932	2.03
	Om+fractures	33.8	64.7	196	9.36	17.9	54.1	5.38	10.3	31.1
	Micas	2.10	3.21	6.66	0.901	1.38	2.86	0.626	0.959	1.97

Table 2. REA values in mm, calculated for different number of domains and for the phases of each lamina.

REA were calculated for a number of samples of 1, 5 and 10 and for $\varepsilon_{rel} = 0.05$, 0.1 and 0.15 (Table 2) according to Table 1 and Fig. 8. For $\varepsilon_{rel} << 0.05$, unrealistically high values of REA were found, significantly greater than lamina width. Therefore, these values were not considered to be realistic. The REA calculated for $\varepsilon_{rel} = 0.1$ and $N = 1$ are millimetric surfaces. However, the maximum possible lamina width used to calculate the microstructural parameters is only 1.5 mm due to natural sedimentary structure (Fig 2). As such, the calculations for $N = 10$ and $\varepsilon_{rel} = 0.1$ are more realistic than for $N = 1$ or 5 because the REA are below 1.5 mm for all phases, except organics and fractures in the gradual organic-matter poor lamina owing to their small quantities and scattered structure.

Randomness of phase distribution

The variance of phase area fraction describes a log-linear law as a function of *D* for both laminae (Fig. 9, equation 6).

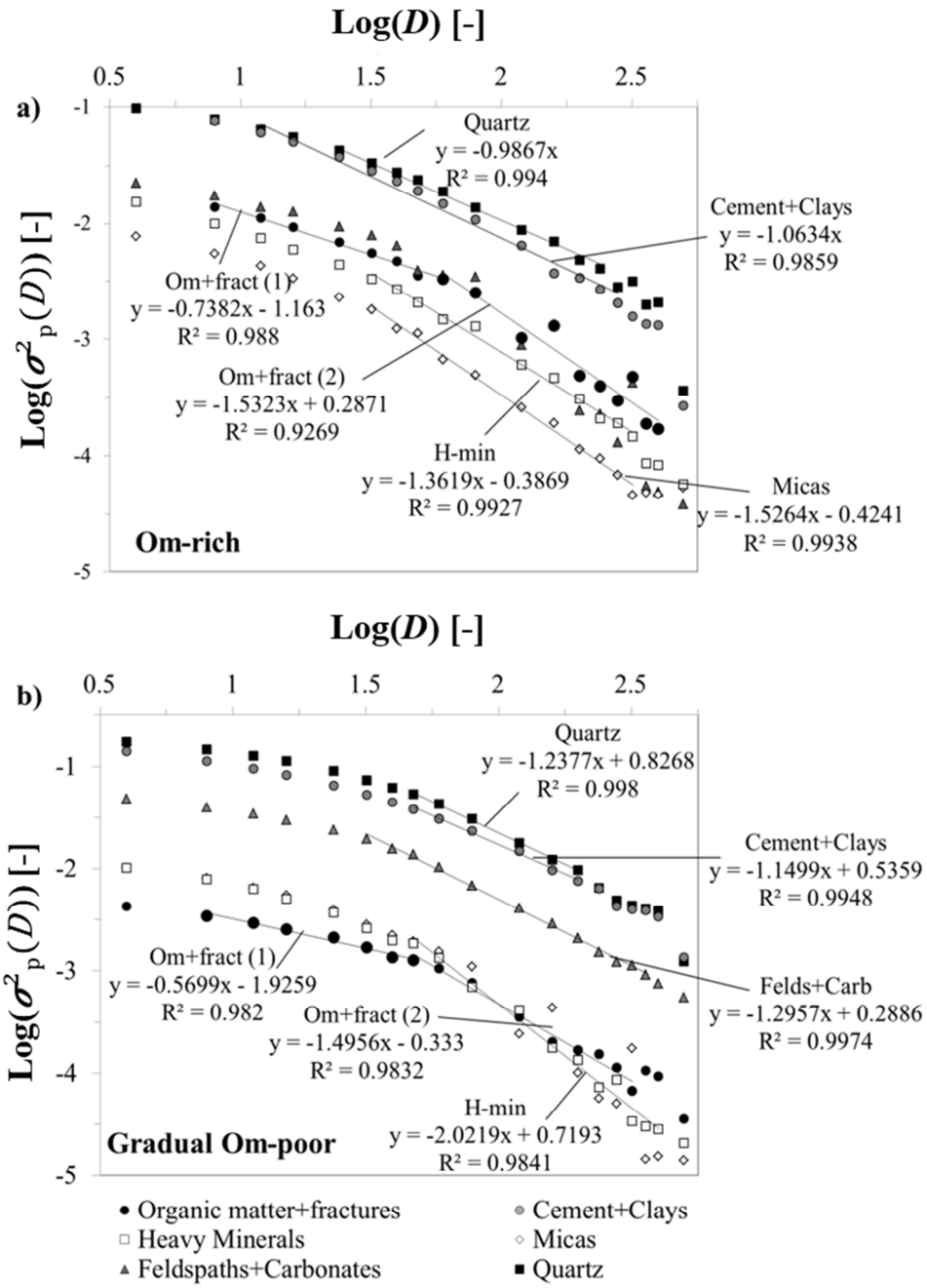

503

504 **Fig. 9. Fitting of Log ($\sigma^2(D)$) as a function of Log (D) for the mineral phases of a) the**

505 **organic-rich lamina and b) the gradual organic-poor lamina.**

$$Log(\sigma_p^2) = -\alpha Log(D) + k \quad (6)$$

506 α in Equation 6 is an indicator of the randomness of the distribution of the physical parameter
507 studied, which is *P* in this study (Cailletaud et al., 1994; Kanit et al., 2003;). According to
508 these authors, *P* was considered to be randomly distributed for $\alpha = 1 \pm 0.15$. $\alpha > 1$ means that
509 the variance increases rapidly with increasing domain, *D*, whereas $\alpha < 1$ when the variance
510 decreases with increasing domain, *D*.

511 In the organic-rich lamina, the proportions of quartz and cement-clays are distributed
512 randomly enough for $D = 24$ to 400 µm ($\log(D)$=1.38 to 2.6) and $D = 12$ to 400 µm
513 ($\log(D)$=1 to 2.6) respectively, unlike the other phases (Fig. 9a). In the gradual organic-poor
514 lamina, only the fraction of cement-clays is randomly distributed for $D = 48$ to 200 µm
515 ($\log(D)$=1.68 to 2.3) whereas all other phases are heterogeneously scattered, with $\alpha >> 1$ for
516 a domain larger than 48 µm. For all phases, the coefficients α are higher in the gradual
517 organic-matter poor lamina than in the organic-matter rich lamina. Therefore, the variance of
518 their fractions increases more rapidly with increasing *D* in the gradual organic-poor lamina
519 than in the organic-rich lamina. The gradual organic-matter poor lamina contains more large
520 grains and clusters (especially quartz, feldspars and carbonates), and consequently, their
521 number per domain is lower than if they were smaller grains. It thus requires a larger domain,
522 *D*, to generate a homogeneous phase area fraction on a finite surface. In the whole range of
523 *D*, $\log(\sigma^2)$ of area fraction for all phases show affine laws in both laminae, especially visible
524 in the gradual-organic matter poor lamina. An example is given for the organics and fractures
525 (Fig. 9 a, b). For organics and fractures, $\alpha << 1$ for $D \leq 60$ µm ($\log(D)$=1.78), while $\alpha >> 1$
526 for $D > 60$ µm. For $D \leq 60$ µm, the resolution is not sufficient to capture the different sizes of
527 organics and fractures. However, domains larger than 60 µm include various sizes of particles
528 heterogeneously scattered and/or with insufficient mean fraction to cause a sharp increase of
529 variance as a function of *D*. The log-linear law is divided in two slopes, caused by a scaling
530 effect due to various particle sizes, but a fixed resolution.

Covariance

In order to compare the different covariograms, they are plotted minus the square of the mean phase area fraction in each lamina in Figure 10.

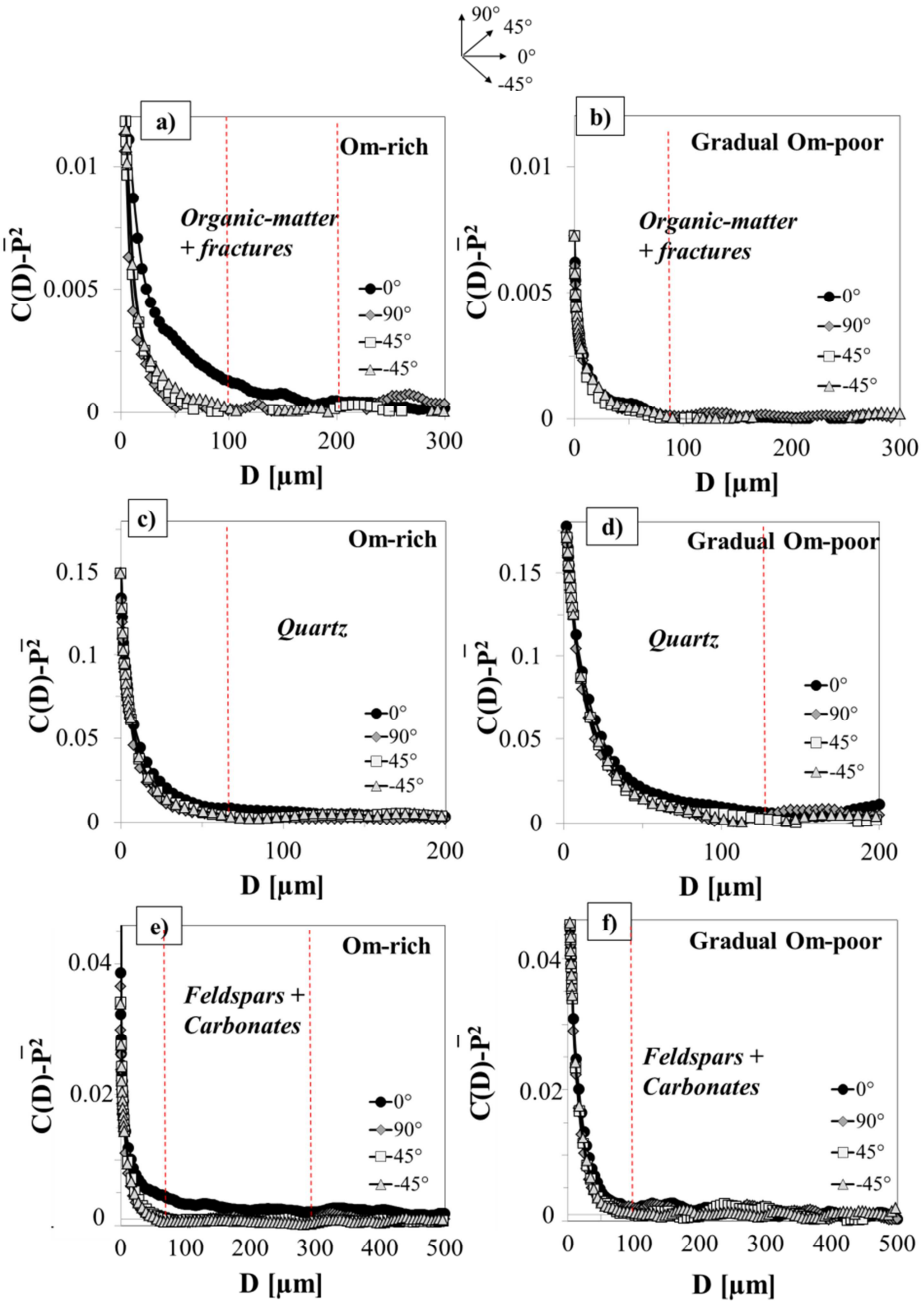

Fig. 10. Covariograms of a) organic-matter and fractures in the Om-rich lamina; b) organic-matter and fractures in the gradual Om-poor lamina; c) quartz in the Om-rich

lamina; d) quartz in the gradual Om-poor lamina; e) feldspars and carbonates in the gradual Om-poor lamina; and f) feldspars and carbonates in the Om-rich lamina.

Organic-matter and fractures become homogeneously scattered for $D \geq 100$ µm, except in the 0° orientation with $D \geq 200$ µm, due to horizontal fractures and elongated particles of organics in the organic-matter rich lamina (Fig. 10a, b). Under the study conditions, domains smaller than 100 µm can be considered as heterogeneous scales for the organic-poor lamina, and 200 µm for the organic-rich lamina. The covariograms of quartz reach the asymptote for domains $D \geq 75$ µm in the organic-matter rich lamina and 120 µm in the gradual organic-poor lamina (Fig. 10 c, e). The higher heterogeneous scale relative to quartz in the gradual organic-poor lamina is mainly due to the presence of aggregates which contribute towards an increase in the size of quartz heterogeneities.

In the gradual organic-poor lamina, the covariograms of feldspars and carbonate reach the asymptote for D close to 100 µm in all directions, showing a microstructure close to isotropic for these phases at the resolution of the study. However, this is not the case for the organic-rich lamina. The asymptote is reached for D=300 µm in the horizontal direction (0°) contrary to the other directions (asymptotes at 75 µm), due to smaller, more elongate and horizontally-elongate feldspars, as well as horizontal calcite grains within a vein in the organic-rich lamina (bottom part of the lamina, Fig. 2). Therefore, the laminae have different scales of textural heterogeneities. For the microstructure models, the parameters are calculated over a surface of 1.32×1.76 mm^2; at least 3 to 11 times the size of the minimal homogeneous surfaces determined by the covariograms (considering all directions). In the sample of Lower Bowland Shale used here, the variability of microstructure thus causes a variability of the minimum size of the homogeneous scale. Covariograms also indicate that the anisotropy of the microstructure is mainly caused by the organic-matter particles, fractures, feldspars and

carbonates in the organic-rich lamina (Fig. 10 a, c, e). The microstructure is more isotropic in the gradual organic-poor lamina (Fig. 10 b, d, f).

5. Microstructural modelling

The total grain geometry of the model was calibrated against the geometry of all mineral types combined. This calibration, performed against distributions of elongation ratio and orientation, leads to the total distribution of all phases in the model, including the ones that eventually make up the cement and clays. Results of this first step are given in Fig. 11. The overall properties are calibrated at $\xi = 1.3$ in the organic-rich lamina and $\xi = 1.1$ in the gradual organic-poor lamina. ξ is higher for the organic-rich lamina because of particles that are more horizontally-elongated in the organic-rich lamina which therefore cause a greater stretching of the modelled microstructure.

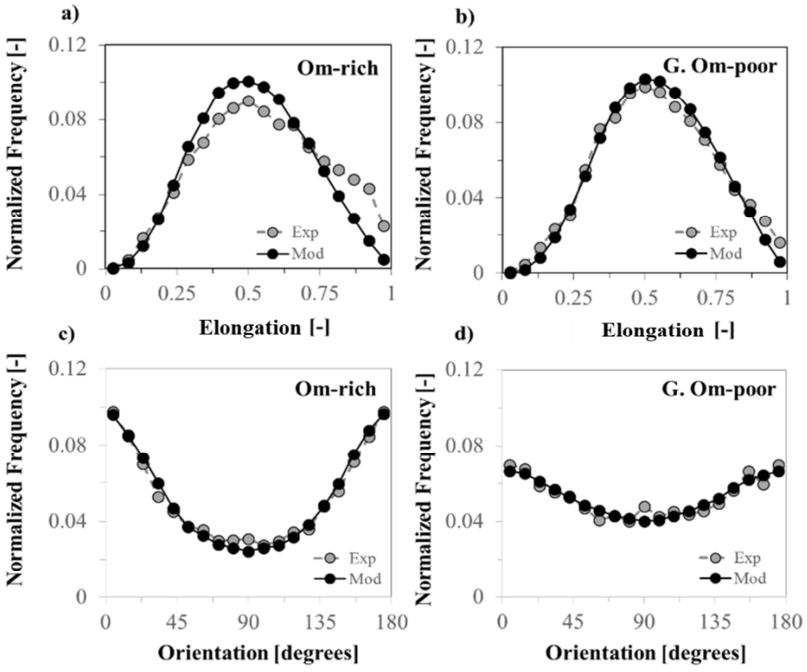

Fig. 11. Result of the model calibration of all model grains against the data of all phase units combined [quartz + (feldspars,carbonates) + micas + heavy-minerals + (organics,fractures)]: a) elongation distributions of the organic-rich lamina; b)

elongation distribution of the gradual organic-poor lamina; c) orientation distribution of the organic-rich lamina; and d) orientation distribution of the gradual organic-poor lamina.

The distributions for elongation and orientation of the microstructure model match well the experimentally observed distributions in the case of all phases combined (Fig. 11). Only the distribution of the elongation of the grains in the organic-rich lamina appears poorly calibrated (Fig. 11a), but this can be corrected for in the model through proportionally assigning mineral properties.

Figure 12 shows two resulting periodic microstructures, reproducing the distributions of elongation, orientation and surface fractions of the gradual organic-matter poor lamina (Fig. 12a) and the organic-matter rich lamina (Fig. 12b). Other periodic microstructures are given in Appendix 1 and the distributions of elongation ratio and orientation for each mineral type are shown in Appendix 2.

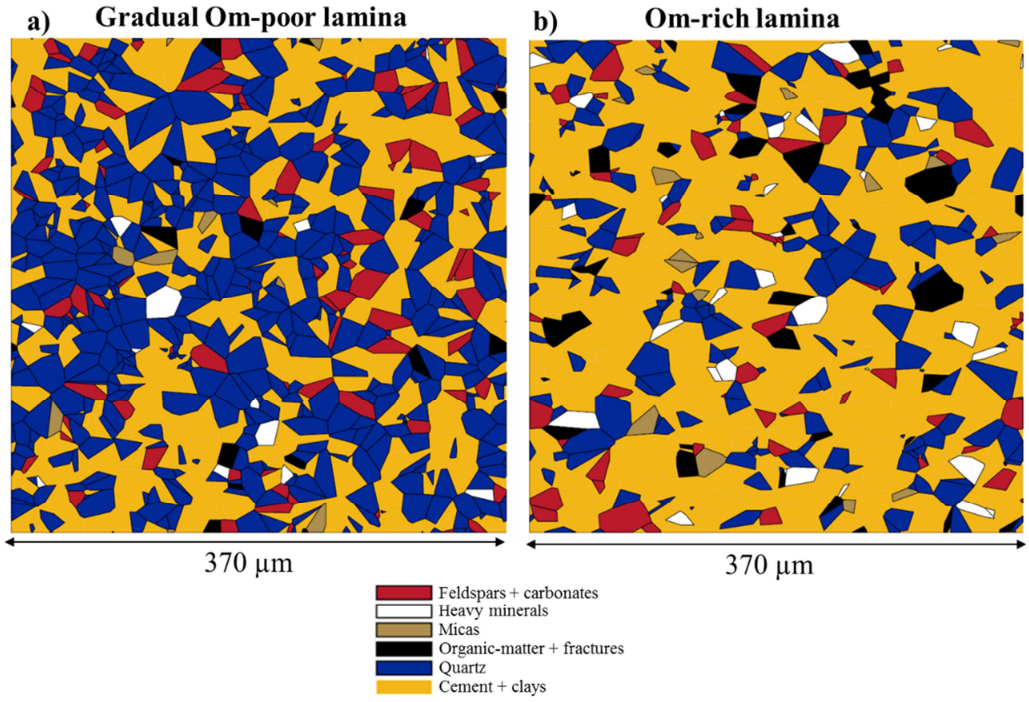

590 **Fig. 12. Geometrical microstructure models of a) the gradual organic-poor lamina, b)**
591 **the organic-rich lamina. The models were generated from 1000 cells of all phases**
592 **combined.**

593 In a numerical sense, a scale bar should not be displayed with the microstructure model.
594 However, shales are multi-scale materials with components and properties varying over this
595 same range of scales. The scale is therefore important in order to determine which
596 phenomena can be studied with these models, because in shale materials phenomena
597 associated with one scale can exhibit controls over behaviors on larger scales. The models
598 presented here are at the mesoscopic scale, effectively micrometric rigid inclusions within a
599 "binder" composed of clays and quartz cement. A scale was qualitatively calculated for the
600 microstructure models in Fig. 12. Considering the mean cell size for each phase and 1000
601 cells in total, the scale value suggested and shown on Fig. 12 is around 370 µm for both
602 laminae.

603 # 6. Discussion

604 ## 6.1. Variability of interfaces relative to phase area fraction, from the µm to
605 mm scale

606 Microstructural defects influence the initiation, propagation and aperture of fractures within
607 shales (Montes et al., 2002; Hedan et al., 2012; Fauchille et al., 2014, 2016; Wei et al., 2016).
608 The maps of phase area fractions highlight the location of three types of interface: the limits
609 between (1) individual grains and the cement and clay phases (micrometer scale), (2)
610 discontinuous phase aggregates and the background (several tens of micrometer scale), and
611 (3) the transitions between laminae (millimeter scale). These interfaces are detected as a
612 function of the size of the calculation domain, which is directly correlated to the scale

investigated. The capture of these different interfaces is only possible with a large mosaic of images in high resolution, which allows a multi-scale investigation of the microstructure. Multi-scale 2D mapping allows the detection of heterogeneities and interfaces which may not be obvious when only examining at the initial mosaic, especially for aggregate boundaries.

The Lower Bowland Shale has a complex and multi-scale natural fracture network (Fauchille et al., 2017). The Lower Bowland Shale sample studied here may have also an interesting potential for "artificial" (such as hydraulic simulation) fracture propagation in multiple directions, due to the variability of interfaces relative to the microstructure.

The transport properties of shales are controlled by the structure and arrangement of potential transport pathways (Keller et al., 2011), particularly at the nanoscale (McKernan et al., 2017). Microcrack location and properties are important for any bottom-up prediction of the transport properties of shales. The quantification of strain concentrations at specific interfaces using digital image or volume correlation may present an interesting way forward in the development of predictive models of fracture initiation and propagation, and in the understanding of scale factors controlling the fracture mechanisms.

6.2. Contrasting vertical microstructural properties in the Lower Bowland Shale, from the µm to mm scale

According to previous studies, the qualitative variability of microtexture of Bowland Shale from Preese-Hall-1 lies at the borehole scale with various microtexture types (Andrews, 2013; Fauchille et al., 2017). Here, we demonstrate quantitatively that it is also variable at the sample scale, from the mm to the µm at the resolution used. The alternation of mineralogically and texturally variable laminae indicates periodic changes of depositional controls during the sedimentation process.

With different mineral content, grain properties and anisotropy, the laminae may have markedly different mechanical properties and fracturing behavior, both within each layer, but perhaps particularly at their transitions, which are smooth or abrupt, but necessarily elastically contrasting. These different properties and behavior could influence the production and orientation of microcracks that are likely to control permeability and contribute significantly to anisotropy (McKernan et al., 2017). The organic-poor lamina is quartz-rich (detrital quartz and cement), unlike the organic-rich lamina. A relatively low proportion of clay minerals (<35%) (Andrews, 2013) and high proportion of non-swelling minerals is considered to be favorable for hydraulic fracturing cutting across the layering (Jarvie, 2012, 2014), depending on the in-situ stress state, and hence for potential gas extraction. High proportions of quartz or carbonates that are contiguous limit ductility and enhance the brittleness of the rock (Jarvie 2014; Raji et al., 2015). Microtextural changes across layers induce discontinuities and weak regions, producing localized stresses, and strain incompatibilities under mechanical simulations (Lan et al., 2010 ; Amann et al., 2011) which aid in the development of pathways for fracture growth.

However, the presence of a laminated structure can act to limit the vertical extent of fractures by blunting cracks propagating across the layering. Ease of formation of shear steps parallel to laminae further acts to inhibit vertical fracture growth by blocking upward flow paths for hydraulic fracture fluid (Rutter and Mecklenburgh, 2017). The presence of rather thin laminae increases the number of interfaces relative to thick beds, and thereby improves the number of potential pathways for fracturing. At such larger scales, in the Austin Chalk for example, the vertical connectivity of fractures is controlled by the vertical alternation of chalk and shale layers due to different microstructure (grain size), fracture toughness and maximum compressive stress (Warpinski and Teufel, 1989; Rijken and Cooke, 2001). According to previous studies, the Bowland Shale contains laminated and interlaminated microtexture

types with laminae less than millimeter-thick. Note that the thickness of laminae is much smaller and periodic in the interlaminated microtexture than the laminated microtexture. Thinner shale layers have lower resistance to fracturing compared to thick beds (Rijken and Cooke, 2001). The characterization of the mechanical behavior of each type of lamina will aid understanding of the impact of the lamination on the vertical propagation of hydraulic fractures in the Bowland Shale.

6.3. Comparison of various methods for estimating the homogeneous scales of the Bowland Shale microstructure

The counting-box and the covariance methods are easier and faster to perform than the 2D mapping and dispersion approaches of Kanit et al., (2003) which are more time-consuming due to the requirement for incremental calculations on millions of pixels. Even if the center of the first domain can be chosen randomly, the counting-box method gives a local approximation of the representative area of the total surface investigated, for specific physical parameters, scale and resolution. Nevertheless, the results depend strongly on the final surface because the comparative surfaces overlap. For example, the domains of 1 and 1.2 mm have an overlap of 83.3% ($100 \times 1/1.2 = 83.3$ %). As the calculation domain becomes closer to the final surface (i.e. 1.76 × 1.32 mm in this case), the probability that the physical parameter (area fraction here) measured on the subsurface is close to the mean parameter of the entire surface increases and reaches 1.

In the dispersion approach, or mosaic scattering, the mosaic is divided into tens to several thousands of independent domains which give a sufficient set of data for statistical interpretation. The domains are compared to each other, rather than to a mean parameter measured over the whole surface. However, the requirement for this substantial number of subareas does not allow the use of areas larger than 400 × 400 µm in our case, whereas

calculations are performed for millimeter-scale areas in the counting-box and covariance approaches. The dispersion approach therefore limits the maximum size of the subareas used. The representative areas are thus determined by extrapolation using a power law and not directly from experimental data.

For each phase unit considered independently from the others, the homogeneous surfaces of phase area fraction are obtained at 1-1.2 mm with a relative error of 10% with the counting box, whereas they are 7 to 9 mm with the dispersion approach. For all phase units combined, the homogeneous areas are much smaller due to a balance effect caused by the mixing of low proportion phases. REA are in the range of 150-350 µm with the counting box method, whereas they are around 1.44 mm with the dispersion approach for all phases combined to form a single phase. As per previously, the REA are up to 9 times larger with the dispersion approach than with the counting box. The 2D quantitative maps (Figure 4, Appendix A) confirm that the homogeneous surfaces are larger than 500×500 µm for the organic-rich lamina, and larger than 750×750 µm for the organic-poor lamina, which support using the dispersion approach to estimate the REA. The counting box was found to underestimate the size of the representative elementary surface. The 2D mapping of phase area fraction provides a direct method of viewing the parameter under consideration, therefore is useful in the comparison of methods.

The homogeneous surfaces determined by the covariance approach are much smaller than those obtained by the counting box and dispersion methods (Rolland du Roscat et al., 2007,). Indeed, the covariance is used to define homogeneity relative to the size of objects compriing the image (Fig. 2b), i.e., the characteristic length of heterogeneities, in addition to their area fraction. The size of the homogeneous scales determined by the dispersion approach appears proportional to the number of heterogeneities, with a characteristic length determined by the covariance (Rolland du Roscat et al., 2007).

Therefore, we recommend using the dispersion approach when the surface is large enough to have several sizes of subareas, in order to extrapolate REAs at different relative errors. This is supported by the 2D quantitative maps showing that the counting box and the covariance approaches are not sufficient to define a homogeneous scale of the area fraction on a large surface. The covariance gives a minimum size of homogeneous scale which is important in the case that a larger surface cannot be investigated.

The counting-box and covariance methods are widely used in image analysis, and geoscience generally. On the other hand, the dispersion method introduced by Kanit et al., (2003) has not been very commonly applied in geoscience, and particularly to shales, except for recent studies from Klaver et al., (2012), Keller et al., (2013) and Houben et al., (2014). The results previously explained have shown that this method is robust enough to be applied to a natural and complex material such as shale, and can be applied to numerical and artificial materials as well as natural materials.

The comparison of the phase area fractions for various sizes of domain can also be compared with XRD results, to quantify if the mesoscale can be representative of the macroscale. XRD analyses are performed on a 100 mg powder, but the powder comes from a centimeter-size sample in order to represent as well as possible the macroscale. Area fractions from SEM images represent the mesoscale. However, to compare weight and volume data from XRD with area fractions from SEM images, an accurate 3D characterization of the microstructural anisotropy is ideally required. 3D microstructural data are poorly documented at the mesoscopic scale for the Bowland Shale, despite recent work at the microscale (Ma et al., 2016). This comparison was not possible in this case.

6.4. Using the geometrical microstructure models

The geometrical models generated in this study represent the mesoscale of two laminae of a sample of the Lower Bowland Shale, in which inclusions of quartz, feldspars, carbonates, micas, heavy minerals, organic matter and fractures are embedded in a clay matrix and quartz cement. The cement, clays, organics and microfractures define a porous network which provides potential pathways for gas transport following fracturing stimulation. Frey et al., (2012) and van den Eijnden et al., (2016, 2017) use such microstructures to model the micro and macroscale hydro-mechanical behavior of shale in a finite element squared (FE^2) model, attributing mechanical and petrophysical properties (e.g. stiffness, hydraulic conductivity) to each phase. With microstructural parameters, Houben et al. (2014), Lan et al., (2010) and Guo et al., (2013) also modeled the microstructure of shales and brittle rocks, by quantitative approaches or by using a distinct element code to generate a deformable microstructure.

The model of microstructure of the Bowland Shale presented here can potentially act as a basis for similar hydraulic transfer modeling in the Bowland Shale at the mesoscopic scale. It can be used to upscale the hydromechanical behavior from the microstructure scale to the macroscale taking into account the anisotropy of the small components of the shale material.

Moreover, the geometry of the microstructural model includes two scales: the scale relative to individual grains and the scale of grain aggregates. It can therefore be used with whole representative images or divided in small subareas (smaller “REA”) to study the influence of microstructural heterogeneities (aggregates, individual grains in the cement, grains of feldspars and quartz stacked together…) on the hydromechanical behavior of the material.

6.5. Potential of image mosaics and representative microstructure models for upscaling

Microstructural data are collected at an infinitesimally smaller scale than the size of the Bowland Basin, qualitatively estimated at the kilometer scale (Andrews, 2013). It is mainly

757 due to the fact that microstructural features are currently visible with high resolution
758 techniques such as microscopy and tomography, which do not allow the observation of larger
759 samples than the centimeter-size. However, numerical models for hydraulic fracturing require
760 representative microstructural data from the pore scale to hundreds of meters, which makes
761 upscaling a real challenge. Averages of microstructural parameters at a defined scale can be
762 calculated on representative areas of smaller scales and implemented into numerical
763 calculations at a larger scale (e.g. Wen and Jaime Gomez-Hernandez, 1996; Zhang et al.,
764 2012; Peng et al, 2015). Different methods such as homogenization or multiscale asymptotics
765 can be applied during the approach of upscaling (Khalili et al., 2012; Kazemi et al., 2012;
766 Davit et al., 2013).The geometrical models of the microstructure determined from
767 representative experimental areas have the same area fraction and the same distributions for
768 grain elongation ratio and orientation. However, they do not have the same grain structure
769 (layout). The dispersion method could therefore provide the quantification of the variability
770 of grain layout in those REAs. A standard deviation of particle layout could be used to define
771 a standard of deviation of the upscaled data resulted from these models. A few example
772 geometrical models are given in Appendix.

773 ## 7. Conclusions

774 The microstructure of a laminated sample of Lower Bowland Shale from the Preese-Hall 1
775 borehole was mapped using a mosaic of 2D-SEM images at the mesoscopic scale. The
776 quantitative characterization of the sample's microstructure demonstrates a high vertical
777 variability of mineral content, grain properties and grain shape anisotropy at the millimeter
778 scale from a gradual organic-matter poor lamina to an organic-rich lamina. Quartz, feldspars
779 and carbonate aggregates act to increase the spatial variability inside each lamina. The multi-
780 scale 2D mapping of phase area fraction highlights multi-scale interfaces of area fractions,

781 which are potentially of importance to the understanding of fracture initiation and
782 propagation. The Lower Bowland Shale sample chosen here might have potential for multiple
783 direction fracture propagation due to the high variability of microstructure heterogeneities
784 and interfaces (subject to the anisotropy of the ambient stress field), in addition to a complex
785 natural fracture network that might be re-stimulated.

786 The counting-box, dispersion, covariance and 2D mapping approaches were compared to
787 estimate the representativeness of the microstructure of each lamina, based on the phase area
788 fraction parameter. 2D phase mapping supports the use of the dispersion approach to
789 calculate the REA in such heterogeneous rock on a large surface. Nevertheless the covariance
790 allows the quantification of a minimum homogeneous surface relative to the size of particles.
791 The models of the geometry of the microstructure were built with parameters calculated from
792 thousands of grains on a surface of 1.280×1.682 mm^2, which is 3 to 11 times larger than the
793 maximum size of microstructural heterogeneities according to the four methods. This
794 microstructure model has been shown to be as representative as is possible from a sample of
795 this scale, and could be used as a starting point in the improvement of our understanding of
796 fluid flow through the porous phase in the Bowland Shale at the mesoscopic scale.

797

798 **Acknowledgments**

799 This project was funded in part by the UK-NERC (NE/M001458/1) and the European
800 Union's Horizon 2020 716 Research and Innovation Programme under the
801 ShaleXenvironmenT project (grant no. 640979). Facilities at the Research Complex at
802 Harwell are gratefully acknowledged, supported in part by the UK-EPSRC (EP/I02249X/1).
803 Data Statement: representative research data is presented in the images and graphs in this
804 manuscript. Other datasets generated and/or analyzed during this study are not publicly

available due to their large size but are freely available from the corresponding author on reasonable request.

Appendices:

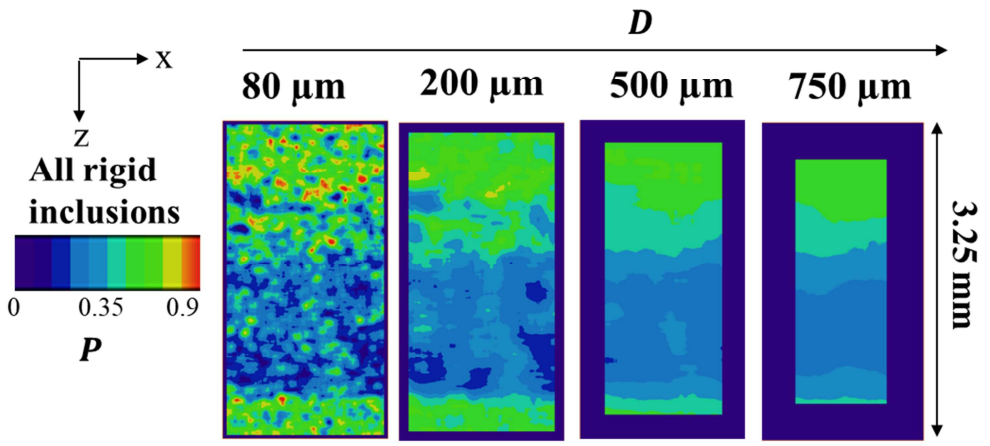

Appendix 1 : Quantitative maps of the local area fraction for all rigid inclusions in the cement (quartz+carbonates+feldspars+micas+heavy minerals+organics+fractures), as a function of the size of the calculation domain *D*.

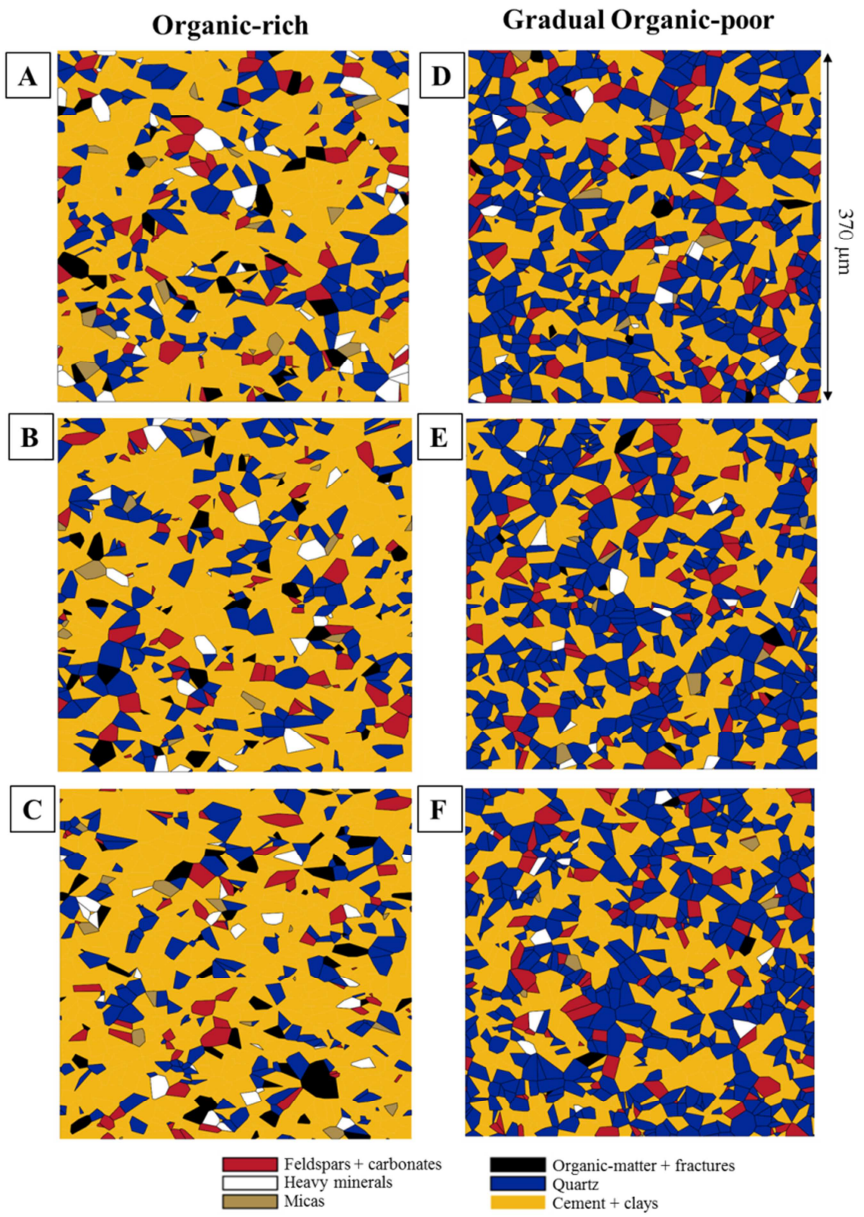

Appendix 2 : Example models of the geometry of the microstructure in the Lower Bowland Shale: A,B,C are random microstructures for the organic-rich lamina and D,E,F for the organic-poor lamina.

References

Al-Raoush, R. and Papadopoulos, A. 2010. Representative elementary volume analysis of porous media using X-ray computed tomography. *Powder technology*, 200, 69-77.

820 Amann, F., Button, E.A., Evans, K.F., Gischig, V.S. and Blümel, M. 2011. Experimental study of
821 the brittle behavior of clay shale in rapid unconfined compression. *Rock mechanics and rock*
822 *engineering*, 44(4), 415-430.

823 Amann, F., Ündül, Ö., and Kaiser, P. K. 2014. Crack initiation and crack propagation in
824 heterogeneous sulfate-rich clay rocks. *Rock Mechanics and Rock Engineering*, 47(5),
825 1849-1865.

826 Andrews, I. J. 2013. The Carboniferous Bowland Shale gas study: geology and resource
827 estimation. NERC report.

828 Bear, J. 1972. Dynamics of fluids in porous media. Elsevier, New-York, NY, USA, 764.

829 Bear, J. and Bachmat, Y. 1984. Transport phenomena in porous media-basic equations. In
830 Bear, J., Corapeioglu, M.Y., Eds., Fundamentals of Transport Phenomena in Porous
831 Media. NATO ASI Series, 82, 3-61.

832 Berger, J.O. 2013. *Statistical decision theory and Bayesian analysis*. Springer Science &
833 Business Media.

834 Bernard, S., Horsfield, B., Schulz, H.M., Schreiber, A., Wirth, R., Vu, T.T.A., Perssen, F.,
835 Könitzer, S., Volk, H., Sherwood, N. and Fuentes, D. 2010. Multi-scale detection of
836 organic and inorganic signatures provides insights into gas shale properties and
837 evolution. *Chemie der Erde-Geochemistry*, 70, 119-133.

838 Bernardo, J.M. and Smith, A.F. 2001. Bayesian theory.

839 Berryman, J.G. and Blair, S.C. 1986. Use of digital image analysis to estimate fluid
840 permeability of porous materials: application of two-point correlation functions. *J. Appl.*
841 *Phys*. 60:1930–1938. doi: 10.1063/1.337245.

842 Boger, F., Feder, J., Jossang, T. and Hilfer, R. 1992. Microstructural sensivity of local
843 porosity distributions. *Physica A: Statistical Mechanics and its Applications*, 187 (1-2),
844 55-70.

845 Bonnelye, A., Schubnel, A., David, C., Henry, P., Guglielmi, Y., Gout, C., Fauchille, A.L.
846 and Dick, P. 2017a. Strength anisotropy of shales deformed under uppermost crustal
847 conditions. *Journal of Geophysical Research: Solid Earth*, *122*(1), 110-129.

848 Bonnelye, A., Schubnel, A., David, C., Henry, P., Guglielmi, Y., Gout, C., Fauchille, A.L.
849 and Dick, P., 2017b. Elastic wave velocity evolution of shales deformed under
850 uppermost crustal conditions. *Journal of Geophysical Research: Solid Earth*, *122*(1),
851 130-141.

852 Cailletaud, G., Jeulin, D. and Rolland, P. 1994. Size e□ect on elastic properties of random
853 composites. *Engng. Computat*. 11, 99–110.

854 Cosenza, P., Prêt, D. and Zamora, M. 2015. Effect of the local clay distribution on the
855 effective electrical conductivity of clay rocks. *Journal of Geophysical research: solid*
856 *Earth*, 120(1), 145-168.

857 Davit, Y., Bell, C. G., Byrne, H. M., Chapman, L. A., Kimpton, L. S., Lang, G. E., ... &
858 Waters, S. L. (2013). Homogenization via formal multiscale asymptotics and volume
859 averaging: How do the two techniques compare? *Advances in Water Resources*, 62, 178-
860 206.

861 Degallaix, S. and Ischner, B. 2007. Caractérisation expérimentale des matériaux: propriétés
862 physiques, thermiques et mécaniques, vol.2., PPUR Presses Polytechniques.

863 De Pater, C.J. and Baisch, S. 2011. Geomechanicla Study of Bowland shale seismicity,
864 *synthesis report* 57. Cuadrilla resources.

EIA (US) 2013. Technically recoverable shale oil and shale gas resources: an assessment of 137 shale formations in 41 countries outside the United States. Report June 2013.

EIA, (US) 2015a. Technically recoverable shale oil and shale gas resources: United Kingdom. Report September 2015.

Fan, Z., Wu, Y., Zhao, X. and Lu, Y. 2004. Simulation of polycrystalline structure with Voronoi diagram in Laguerre geometry based on random closed packing of spheres. *Computational Materials Science*, 29(3), 301-308.

Fauchille, A.L., Hedan, S., Prêt, D., Valle, V., Cabrera, J. and Cosenza, P. 2014. Relationships between desiccation cracking behavior and microstructure of the Tournemire clay rock by coupling DIC and SEM methods. *Proceedings of IS on Geomechanics from Micro to Macro, Cambridge*, UK; CRC Press/Balkema: Leiden, The Netherlands.

Fauchille, A.L., Hedan, S., Valle, V., Prêt, D., Cabrera, J. and Cosenza, P., 2016a. Multi-scale study on the deformation and fracture evolution of clay rock sample subjected to desiccation, *Applied Clay Science*, 132, 251-260.

Fauchille, A. L., Hedan, S., Valle, V., Pret, D., Cabrera, J., and Cosenza, P. 2016b. Relationships between cracking, strains and proportions of clay matrix and rigid inclusions in Tournemire clay rock, *Proceedings of the 2nd Petrus Opera Conference on Radioactive Waste Management and Geological Disposal*, June 2016, Delft, Netherlands.

Fauchille, A.L., Ma, L., Rutter, E., Chandler, M., Lee, P.D. and Taylor, K.G. 2017. An enhanced understanding of the Basinal Bowland shale in Lancashire (UK), through

microtextural and mineralogical observations. *Marine and Petroleum Geology*, 86, 1374-1390.

Figueroa Pilz, F., Dowey, P.J., Fauchille, A.L., Courtois, L., Bay, B., Ma, L., Taylor, K.G., Mecklenburgh, J. and Lee, P.D., 2017. Synchrotron tomographic quantification of strain and fracture during simulated thermal maturation of an organic□rich shale, UK Kimmeridge Clay. *Journal of Geophysical Research: Solid Earth*, *122*(4), 2553-2564.

Gaboreau, S., Robinet, J.-C. and Prêt, D. 2016. Optimization of pore-network characterization of a compacted clay material by TEM and FIB/SEM imaging. *Microporous and Mesoporous Materials*, 224, 116-128.

Gawthorpe, R.L. 1987. Tectono-sedimentary evolution of the Bowland Basin, northern England, during the Dinantian. *Journal of the Geological Society (London)*, 144, 59-71.

Grolier, J., Fernandez, A., Hucher, M. and Riss, J. 1991. *Les propriétés physiques des roches, Théories et Modèles*, Ed. Masson, 197.

Guo, Z., Li, X.Y., Liu, C., Feng, X. and Shen, Y. 2013. A shale rock physics model for analysis of brittleness index, mineralogy and porosity in the Barnett Shale, *J. Geophys. Eng.*, 10, 025006.

Hédan, S., Cosenza, P., Valle, V., Dudoignon, P., Fauchille, A. L., and Cabrera, J. 2012. Investigation of the damage induced by desiccation and heating of Tournemire argillite using digital image correlation. *International Journal of Rock Mechanics and Mining Sciences*, 51, 64-75.

Houben, M.E., Desbois, G. and Urai, J.L. 2014. A comparative study of representative 2D microstructures in Shale and Sandy facies of Opalinus Clay (Mont Terri, Switzerland) inferred from BIB-SEM and MIP methods. *Mar. Pet. Geol*. 49, 143–161.

910 Houben, M.E., Barnhoorn, A., Wasch, L., Trabucho-Alexandre, J., Peach, C.J. and Drury,
911 M.R. 2016. Microstructures of Early Jurassic (Toarcian) shales of Northern Europe,
912 *International Journal of Coal Geology*, 165, 76-89.

913 Jaeger, J.C. and Cook, N.G.W. 1976. Fundamentals of Rock Mechanics, *second ed. Chapman*
914 *and Hall*, London.

915 Jarvie, D. M., 2012. Shale resource systems for oil and gas: Part 1—Shale-gas resource
916 systems, in J. A. Breyer (ed.). Shale reservoirs—Giant resources for the 21st century.
917 AAPG Memoir 97: 69– 87.

918 Jarvie, D.M. 2014. Components and processes affecting producibility and commerciality of
919 shale resource systems. *Geologica Acta: an international earth science journal*, 12(4).

920 Josh, M., Esteban, L., Delle Piane, C., Sarout, J., Dewhurst, D. N., and Clennell, M. B. 2012.
921 Laboratory characterisation of shale properties. *Journal of Petroleum Science and*
922 *Engineering*, 88, 107-124.

923 Kanit, T., Forest, S., Galliet, I., Mounoury, V. and Jeulin, D. 2003. Determination of the size
924 of the representative volume element for random composites: statistical and numerical
925 approach. *International Journal of solids and structures*, 40(13), 3647-3679.

926 Kameda, A., Dvorkin, J., Keehm, Y., Nur, A. and Bosl, W. 2006. Permeability-porosity
927 transforms from small sandstone fragments. *Geophysics* 71 (1), N11-19.

928 Kazemi, A., Shaikhina, D.S., Pickup, G.E., Corbett, P.W., 2012. Comparison of Upscaling
929 Methods in a Heterogeneous Carbonate Model, *SPE Europec/EAGE Annual Conference.*
930 *Society of Petroleum Engineers*.

931 Khalili, A., Arns, C., Arns, J.-Y., Hussain, F., Cinar, Y., Pinczewski, W., Latham, S., Funk,
932 J., 2012. Permeability Upscaling for Carbonates from the Pore-Scale Using Multi-Scale
933 Xray-CT Images, *SPE/EAGE European Unconventional Resources Conference &*
934 *Exhibition-From Potential to Production*.

935 Keller, L.M., Holzer, L., Wepf, R. and Gasser, P. 2011. 3D geometry and topology of pore
936 pathways in Opalinus clay: Implications for mass transport. *Applied Clay Science*, 52,
937 85-95.

938 Keller, L.M., Holzer, L., Schuetz, P. and Gasser, P. 2013a. Pore space relevant for gas
939 permeability in Opalinus clay: Statistical analysis of homogeneity, percolation, and
940 representative volume element. *Journal of Geophysical Research: Solid Earth*, 118,
941 2799-2812.

942 Keller, L.M., Schuetz, P., Erni, R., Rossell, M.D., Lucas, F., Gasser, P. and Holzer, L. 2013b.
943 Characterization of multi-scale microstructural features in Opalinus Clay. *Microporous*
944 *and Mesoporous Materials*, 170, 83-94.

945 Keneti, A., and Wong, R.C.K. 2010. Investigation of Anisotropic Behavior of Montney Shale
946 Under Indirect Tensile Strength Test. In: *Canadian Unconventional Resources and*
947 *International Petroleum Conference*. Society of Petroleum Engineers.

948 Khan, M.W. 2014. A survey: image segmentation techniques. *International Journal of Future*
949 *Computer and Communication*, 3(2), 89.

950 Klaver, J., Desbois, G., Urai, J.L. and Littke, R. 2012. BIB-SEM study of the pore space
951 morphology in early mature Posidonia Shale from the Hils area, Germany. *International*
952 *Journal of Coal Geology*, 982 (103), 12-25.

Klaver, J., Desbois, G., Littke, R. and Urai, J.L. 2015. BIB-SEM characterization of pore space morphology and distribution in postmature to overmature samples from the Haynesville and Bossier Shales. *Marine and Petroleum Geology*, 59, 451-466.

Lan, H., Martin, C.D. and Hu, B. 2010. Effect of heterogeneity of brittle rock on micromechanical extensile behavior during compression loading. *Journal of Geophysical Research: Solid Earth*, *115* (B1).

Ma, L., Taylor, K.G., Lee, P.D., Dobson, K.J., Dowey, P.J. and Courtois, L. 2016. Novel 3D centimetre-to nano-scale quantification of an organic-rich mudstone: The Carboniferous Bowland Shale, Northern England. Marine and Petroleum Geology, 72, 193-205.

Ma, L., Fauchille, A.L., Dowey, P., Figueroa Pilz, F., Courtois, L., Taylor, K.G. and Lee, P.D. 2017. Correlative multi-scale imaging of shales: a review and future perspectives, *Special Publication in the Journal of Geological Society* (London), 454.

McKernan, R., Mecklenburgh, J., Rutter, E. and Taylor, K. 2017. Microstructural controls on the pressure-dependent permeability of Whitby mudstone, *Geological Society London, Special Publications*, 454, 39-66.

Peng, S., Yang, J., Xiao, X., Loucks, B., Ruppel, S. C., and Zhang, T. 2015. An integrated method for upscaling pore-network characterization and permeability estimation: example from the Mississippian Barnett shale. *Transport in Porous Media*, 109(2), 359-376.

Peters, C.A. 2009. Accessibilities of reactives minerals in consolidated sedimentary rock: An imaging study of three sandstones, *Chemical Geology* 265, 198-208.

Prêt, D., Sammartino, S., Beaufort, D., Fialin, M., Sardini, P., Cosenza, P. and Meunier, A. 2010a. A new method for quantitative petrography based on image processing of

chemical element maps: Part II. Semi-quantitative porosity maps superimposed on mineral maps. *American Mineralogist*, 95, 1389-1398.

Prêt, D., Sammartino, S., Beaufort, D., Meunier, A., Fialin, M. and Michot, L.J. 2010b. A new method for quantitative petrography based on image processing of chemical element maps: Part I. Mineral mapping applied to compacted bentonites. *American Mineralogist*, 95, 1379-1388.

Raji, M., Gröcke, D.R., Greenwell, H.C., Gluyas, J.G. and Cornford, C. 2015. The effect of interbedding on shale reservoir properties. *Marine and Petroleum Geology*, 67, 154-169.

Rijken, P. and Cooke, M.L. 2001. Role of shale thickness on vertical connectivity of fractures: application of crack-bridging theory to the Austin Chalk, Texas. *Tectonophysics*, *337*(1), 117-133.

Robinet, J.C., Sardini, P., Coelho, D., Parneix, J.C., Prêt, D., Sammartino, S., Boller, E. and Altmann, S. 2012. Effects of mineral distribution at mesoscopic scale on solute diffusion in a clay-rich rock : Example of the Callovo-Oxfordian mudstone (Bure, France). *Water Resources Research,* 48, 1-17.

Rudge, J.F., Holness, M.B., and Smith, G.C. 2008. Quantitative textural analysis of packings of elongate crystals. Contrib. Mineral Petrol, 156, 413-429.

Rutter, E., and Mecklenburgh, J. 2017. Hydraulic conductivity of bedding-parallel cracks in shale as a function of shear and normal stress. In : *E.H. Rutter, J. Mecklenburgh and K.G. Taylor (Eds.), Geomechanical and Petrophysical Properties of Mudrocks, Geological Society, London, Special Publications*, 454, 67-84.

Sayers, C.M., 2013. The effect of anisotropy on the Young's moduli and Poisson's ratios of shales. *Geophysical Prospecting*, 61(2), 416-426.

999 Sellers, E. and Napier, J. 1997. A comparative investigation of micro-flaw models for the
1000 simulation of brittle fracture in rock. *Computational mechanics*, 20(1), 164-169.

1001 Sone, H., and Zoback, M. D. 2013. Mechanical properties of shale-gas reservoir rocks—Part
1002 1: Static and dynamic elastic properties and anisotropy. *Geophysics*, 78(5), D381-D392.

1003 Stoyan, D., Kendall, WS. and Mecke, J. 1995. Stochastic geometry and its applications.
1004 Wiley, UK.

1005 U.S. Energy Information Administration (USEIA) 2011. World Shale Gas Resources: an
1006 initial assessment of 14 regions outside the United States. *Report prepared by Advanced*
1007 *Resources International Inc.* www.eia.gov/analysis/studies/worldshalegas/.

1008 van den Eijnden, A.P. 2015. Multiscale modelling of the hydromechanical behaviour of
1009 argillaceous rocks. *PhD thesis*, University of Grenoble-Alpes, France.

1010 van den Eijnden, A.P., Bésuelle, P., Chambon, R. and Collin, F. 2016. A FE 2 modelling
1011 approach to hydromechanical coupling in cracking-induced localization
1012 problems. *International Journal of Solids and Structures*, *97*, 475-488.

1013 van den Eijnden, A.P., Bésuelle, P., Collin, F., Chambon, R. and Desrues, J. 2017. Modeling
1014 the strain localization around an underground gallery with a hydro-mechanical double
1015 scale model; effect of anisotropy. *Computers and Geotechnics*, *85*, 384-400.

1016 VandenBygaart, A.J. and Protz, R. 1999. The representative elementary area REA in studies
1017 of quantitative soil micromorphology, Geoderma, 89, 333-346

1018 Vergès, J.M. and Morales, J.I. 2014. The gigapixel image concept for graphic SEM
1019 documentation. *Applications in archeological use-wear studies*. *Micron*, 65, 15-19.

1020 Vik, B., Bastesen, E. and Skauge, A. 2013. Evaluation of representative elementary volume
1021 for a vuggy carbonate rock—Part: Porosity, permeability, and dispersivity. *Journal of*
1022 *Petroleum Science and Engineering*, 112, 36-47.

1023 Wang, L., 2012. Micro-mechanical experimental investigation and modelling of strain and
1024 damage of argillaceous rocks under combined hydric and mechanical loads. PhD thesis,
1025 Ecole Polytechnique, France.

1026 Wang, L., Bornert, M., Héripré, E., Chanchole, S., Pouya, A. and Halphen, B., 2015.
1027 Microscale insight into the influence of humidity on the mechanical behavior of
1028 mudstones. *Journal of Geophysical Research: Solid Earth*, 120(5), pp.3173-3186.

1029 Wei, X., Duc, M., Hattab, M., Reuschlé, T., Taibi, S. and Fleureau, J.M. 2016. Effect of
1030 decompression and suction on macroscopic and microscopic behavior of a clay
1031 rock. *Acta Geotechnica*, *1*(12), 47-65.

1032 Wen, X.H. and Gómez-Hernández, J.J., 1996. Upscaling hydraulic conductivities in
1033 heterogeneous media: An overview. *Journal of Hydrology*, *183*(1-2), ix-xxxii.

1034 **Figure captions**

1035 Fig. 1. Gray level histogram of the first image of mosaic B8 1-1 (this image corresponds to
1036 the first column and first line of the mosaic) before and after drift correction. 8
1037 Fig. 2. (a) Mineral phase segmentation on the whole mosaic of SEM-BSE images of the
1038 Bowland Shale sample. (b) Magnified view of a region of (a). (c) Original (unsegmented)
1039 back-scattered electron image corresponding to (b). 10
1040 Fig. 3. Vertical variability of the area fraction of each mineral along the z axis of the mosaic,
1041 based on horizontal domains of 500 × 4204 pixels (200 µm × 1.682 mm). 18
1042 Fig. 4. 2D maps of phase area fractions with variable domain sizes for: (a-d) cement+clays,
1043 (e-h) quartz, (i-l) feldspars+carbonates, (m-p) Om+fractures. [Each of the three laminae [(1)
1044 organic-poor lamina, (1') gradual organic-poor lamina, (2) organic-rich lamina] are labelled
1045 on (a). 20
1046 Fig. 5. Grain size and grain number distributions for each of laminae 1' (gradual om-poor)
1047 and 2 (om-rich). 24
1048 Fig. 6. Elongation and orientation distributions for a), b) organic matter particles and
1049 fractures, c), d) quartz, e), f) feldspars and carbonates, on the organic-rich (black plots) and
1050 the gradual organic-poor (gray plots) laminae 2 and 1' respectively. Only grains larger than
1051 10 pixels were considered. 25
1052 Fig.7. (a and b) Ratio between the local phase area fraction P and the mean phase area
1053 fraction $\boldsymbol{P}$ as a function of the size of calculation domain D for the *organic-rich lamina*
1054 where b) is a magnified view of the dashed-line box in a) for $D \leq 400\mu m$. (c and d) show
1055 similar features for the *gradual organic-poor* lamina, where d) is a magnified view of the
1056 dashed-line box in c) for $D \leq 400\mu m$. 27
1057 Fig. 8. Relative uncertainty, $\boldsymbol{\varepsilon rel}$, of area fraction as a function of $\boldsymbol{D}$ for a) the organic-rich
1058 lamina and b) the gradual organic-poor lamina, for $N = 1$. 29
1059 Fig. 9. Fitting of Log ($\sigma^2(D)$) as a function of Log (D) for the mineral phases of a) the
1060 organic-rich lamina and b) the gradual organic-poor lamina. 32
1061 Fig. 10. Covariograms of a) organic-matter and fractures in the Om-rich lamina; b) organic-
1062 matter and fractures in the gradual Om-poor lamina; c) quartz in the Om-rich lamina; d)
1063 quartz in the gradual Om-poor lamina; e) feldspars and carbonates in the gradual Om-poor
1064 lamina; and f) feldspars and carbonates in the Om-rich lamina. 34
1065 Fig. 11. Result of the model calibration of all model grains against the data of all phase units
1066 combined [quartz + (feldspars,carbonates) + micas + heavy-minerals + (organics,fractures)]:
1067 a) elongation distributions of the organic-rich lamina; b) elongation distribution of the
1068 gradual organic-poor lamina; c) orientation distribution of the organic-rich lamina; and d)
1069 orientation distribution of the gradual organic-poor lamina. 36
1070 Fig. 12. Geometrical microstructure models of a) the gradual organic-poor lamina, b) the
1071 organic-rich lamina. The models were generated from 1000 cells of all phases combined. ... 38
1072

1073 **Table captions**

Table 1 : Parameters of the power law fitting, ε rel, as a function of D corresponding to both laminae. 30

Table 2 : REA values in mm, calculated for different number of domains and for the phases of each lamina. 31

Gradual Om-poor	**a**	**b**	**R^2**
Om+fractures	103	0.626	0.97
All grains	5.80	0.556	0.99
Cement+clays	7.54	0.556	0.99
Quartz	10.8	0.610	0.99
Feldpars+Carbonates	29.1	0.635	0.99
Heavy minerals	154	0.906	0.98
Micas	218	0.952	0.90
Om-rich			
Om+fractures	39.8	0.658	0.95
All grains	9.19	0.619	0.99
Cement+clays	4.39	0.619	0.99
Quartz	13.9	0.551	0.99
Feldpars+Carbonates	81.9	0.908	0.91
Heavy minerals	36.6	0.706	0.99
Micas	71.3	0.738	0.99

		REA [mm]								
		N=1			N=5			N=10		
	ε_{rel}	***0.15***	***0.1***	***0.05***	***0.15***	***0.1***	***0.05***	***0.15***	***0.1***	***0.05***
Organic-rich	Cement+clays	0.233	0.449	1.38	0.063	0.122	0.375	0.036	0.070	0.214
	Grains	0.746	1.44	4.40	0.203	0.391	1.20	0.116	0.223	0.685
	Quartz	3.71	7.75	27.2	0.861	1.80	6.33	0.459	0.959	3.37
	Feld+Carb	1.03	1.62	20.4	0.426	0.666	1.43	0.291	0.455	0.975
	H-min	2.41	4.28	11.4	0.771	1.37	3.65	0.472	0.838	2.24
	Om+fractures	4.83	8.94	25.6	1.42	2.63	7.55	0.839	1.55	4.46
	Micas	4.24	7.35	18.8	1.42	2.47	6.32	0.892	1.54	3.95
Gradual Organic-poor	Cement+clays	1.15	2.38	8.28	0.270	0.560	1.95	0.145	0.300	1.04
	Grains	0.715	1.482	5.16	0.168	0.349	1.21	0.090	0.187	0.650
	Quartz	1.10	2.14	6.68	0.295	0.573	1.79	0.167	0.325	1.01
	Feld+Carb	4.02	7.61	22.7	1.13	2.14	6.38	0.655	1.24	3.70
	H-min	2.12	3.32	7.14	0.874	1.37	2.94	0.596	0.932	2.03
	Om+fractures	33.8	64.7	196	9.36	17.9	54.1	5.38	10.3	31.1
	Micas	2.10	3.21	6.66	0.901	1.38	2.86	0.626	0.959	1.97